

Heat Transfer Assessment of Aluminum Alloy Corrugated Naval Ship Deck Panels under VTOL Aircraft Thermal Loads

Kara Elizabeth Crosser

Thesis submitted to the faculty of the Virginia Polytechnic Institute and State University in partial fulfillment of the requirements for the degree of

Master of Science

In

Aerospace Engineering

K. Todd Lowe, Chair

Joseph A. Schetz

Michael K. Philen

08/12/2016

Blacksburg, VA

Keywords: Aluminum Alloy, Digital Image Correlation, Strain, Thermocouple, Convection Coefficient, Heat Transfer

Heat Transfer Assessment of Aluminum Alloy Corrugated Naval Ship Deck Panels under VTOL Aircraft Thermal Loads

Kara Elizabeth Crosser

ABSTRACT

The behavior of aluminum alloy ship deck panels under the thermal loads of Vertical Take-off and Landing (VTOL) capable aircraft has become a question of interest with the introduction of new primarily aluminum alloy ships to the U.S. Naval Fleet. This study seeks to provide an initial investigation of this question by examining the transient transfer of heat through aluminum alloy ship deck panels under application of the local heat transfer similar to that of a VTOL aircraft exhaust plume core in typical operation.

In this study, a jet stream intended to replicate the key physics of the core of a VTOL aircraft plume was impinged onto the upper surface of aluminum alloy corrugated deck panel test specimen. Temperature measurements are taken via thermocouples on the face of the specimen opposite the impingement to evaluate heat transfer through the specimen. This data is used to assess the effects of variation in the geometry of the corrugation between specimen. Qualitative temperature distributions were also gathered on the impingement surface via thermal imaging. A quantitative assessment of the heat paths for transverse and vertical heat transfer was made based on a thermal resistance model, leading to a conceptual description of predominant heat flow paths in the specimen, specifically weld lines between the corrugation and the flat plate surfaces. In support of this, thermal images indicated that the weld lines provided paths for heat to be pulled away from the center of heat application more rapidly than over the rest of the surface. Ultimately, heat transfer through the specimen was found to be more dependent on the flow conditions than the variations in geometry of the deck panels due to the low variation in thermal resistance across the plate. A recommendation is made based upon this observation to use the deck panels similarly to heat exchanges by adding a small amount of through-deck airflow in the areas of high heat load.

Acknowledgements

I would like to thank the many people who have greatly supported me in conducting this study. First and foremost, I would like to thank my advisor, Dr. Lowe for his ever-optimistic perspective and crucial guidance throughout this study and in my graduate career. A special thanks to the other members of my advisory committee, Drs. Schetz and Philen for their insight throughout this study.

I would also like to acknowledge Dr. Judy Conley and my mentors at NSWC-Carderock for providing the motivation for this work. They have also been great mentors and colleagues assisting in my professional development throughout my collegiate career.

Finally, I am very grateful for the assistance of everyone in my research group for day-to-day advice, guidance, and friendship. Special thanks to Dan Cadel, Eric Rolfe, Marcie Stuber, Sean Shea, Tyler Vincent, Will George, and Tamy Guimarães.

Table of Contents

| | |
|--|------|
| Table of Contents | iv |
| List of Figures | vi |
| List of Tables | viii |
| Nomenclature | ix |
| 1. Introduction | 1 |
| 1.1 Background & Motivation | 1 |
| 1.2 Overview | 3 |
| 2. Problem Description and Review of Relevant Literature | 3 |
| 2.1 Review of Subsonic Impinging Jet Characteristics and Zones | 3 |
| 2.2 Heat Transfer Fundamentals | 4 |
| 2.2.1 Heat Transfer Modes: Convection, Conduction, & Radiation | 4 |
| 2.2.2 Convection Heat Transfer Coefficient | 5 |
| 2.2.3 Nusselt number | 6 |
| 2.2.4 Reynolds number | 6 |
| 2.2.5 Lumped Capacitance Method | 6 |
| 2.2.6 Biot Number | 7 |
| 2.2.7 Fourier Number | 7 |
| 2.2.8 Dimensionless Temperature | 7 |
| 2.3 Thermal Loads Generated by VTOL Operations | 8 |
| 3. Experimental Approach | 11 |
| 3.1 Surface Thermocouples | 11 |
| 3.1.1 Thermocouple Configurations & Types | 11 |
| 3.1.2 Contact Resistance | 12 |
| 3.2 Aluminum Alloy Deck Panel Description | 12 |
| 3.3 Virginia Tech Hot Jet Facility | 14 |
| 3.4 Experimental Specimen Mounting Rig | 15 |
| 3.5 Instrumentation | 18 |
| 3.5.1 Temperature Probes | 19 |
| 3.6 Experimental Procedures | 19 |
| 3.6.1 Testing Phase 1 | 20 |
| 3.6.2 Testing Phase 2 | 21 |
| 3.7 Testing Lessons Learned | 23 |

| | |
|---|----|
| 4. Results & Discussion | 24 |
| 4.1 Phase 1 Test Results..... | 24 |
| 4.2 Phase 2 Test Results..... | 28 |
| 4.2.1 Thermocouple Data | 28 |
| 4.2.2 Infrared Images | 35 |
| 4.2.3 Thermal Resistance Model..... | 43 |
| 4.3 Uncertainty Study for Nusselt Number..... | 48 |
| 5. Conclusions | 50 |
| References | 51 |
| Appendix A: Digital Image Correlation..... | 54 |
| A.1 Digital Image Correlation Fundamentals..... | 54 |
| A.1.1 Stereoscopic Imaging..... | 54 |
| A.1.2 DIC Testing Methods..... | 54 |
| A.1.3 Imaging Equipment & Configuration | 56 |
| 3.7.3 Processing and Results of DIC Images..... | 56 |
| Appendix A References | 59 |

List of Figures

| | |
|--|----|
| Figure 1: Cross-section of an Aluminum Alloy Ship Deck Panel..... | 2 |
| Figure 2: Schematic of a Subsonic Circular Jet Impinging on a Flat Surface [6]..... | 4 |
| Figure 3: Nominal V-22 Osprey Stagnation Temperature Profile on Landing Surface [11] | 9 |
| Figure 4: Nominal V-22 Osprey Convection Coefficient Profile on Landing Surface [11]..... | 10 |
| Figure 5: Test Specimen 1. FSW member is along centerline of cross-section | 13 |
| Figure 6: Test Specimen 2. FSW members symmetric about centerline of cross-section..... | 13 |
| Figure 7: Image of Virginia Tech Hot Jet Facility at the Advanced Propulsion and Power Laboratory..... | 15 |
| Figure 8: Schematic of Virginia Tech Hot Jet Facility | 15 |
| Figure 9: Test Specimen Positioned in Experimental Mounting Rig | 16 |
| Figure 10: Side View of Test Specimen Positioned in Experimental Mounting Rig | 17 |
| Figure 11: Overhead View of Equipment and Instrumentation Configuration | 18 |
| Figure 12: Back Surface Thermocouple Configuration Schematic..... | 19 |
| Figure 13: Back Surface Thermocouple Configuration in Relation to Weld Lines for (a) Test Specimen 1 and (b) Test Specimen 2; spacing is not to scale – proper spacing is shown in Figure 12..... | 22 |
| Figure 14: Phase 1 TC 1 Test Results vs. Theoretical Curve | 25 |
| Figure 15: Convection Heat Transfer Coefficient Distribution on the Front Surface of the Steel Plate | 26 |
| Figure 16: Convection Heat Transfer Coefficient Distribution on the Front Surface of the Steel Plate | 27 |
| Figure 17: Phase 2 Test Specimen 1 Thermocouple Data..... | 29 |
| Figure 18: Phase 2 Test Specimen 2 Thermocouple Data..... | 29 |
| Figure 19: Phase 2 TC 1 Data for Each Test Specimen | 30 |
| Figure 20: Phase 2 TC 4 Data for Each Test Specimen | 31 |
| Figure 21: Phase 2 TC 5 Data for Each Test Specimen | 32 |
| Figure 22: Phase 2 TC 7 Data for Each Test Specimen | 33 |
| Figure 23: Phase 2 TC 7 Data for Each Test Specimen | 34 |
| Figure 24: Phase 2 Test Specimen 1 Infrared Image, 40 Minutes into the 60-minute Loading Period | 37 |
| Figure 25: Phase 2 Test Specimen 2 Infrared Image, 40 Minutes into the 60-minute Loading Period | 38 |
| Figure 26: Phase 2 Test Specimen 1 Radial Temperature Distributions, Horizontally along the Centerline | 39 |
| Figure 27: Phase 2 Test Specimen 1 Vertical Temperature Distributions | 40 |
| Figure 28: Phase 2 Test Specimen 2 Radial Temperature Distributions, Horizontally along the Centerline | 41 |
| Figure 29: Phase 2 Test Specimen 2 Vertical Temperature Distributions | 42 |
| Figure 30: Test Specimen 1 Cross-section Thermal Resistance Model..... | 44 |
| Figure 31: Test Specimen 1 Cross-section Thermal Resistance Model..... | 44 |
| Figure 32: Test Specimen 1 Cross-section Thermal Resistance Map from Upper to Lower Surface..... | 45 |
| Figure 33: Test Specimen 2 Cross-section Thermal Resistance Map from Upper to Lower Surface..... | 46 |
| Figure 34: Qualitative Phenomenological Heat Transfer Schematic for Test Specimen 1 | 47 |
| Figure 35: Qualitative Phenomenological Heat Transfer Schematic for Test Specimen 2 | 47 |
| Figure 36: Uncertainty in Nusselt Number at TC 1 on Test Specimen 1 due to Perturbation of Steel Plate Thickness, Fluid Temperature Upstream of the Specimen, and Jet Diameter | 49 |
| Figure A.1: Speckle Pattern on Test Specimen 2 | 55 |
| Figure A1: εxx Strain Map of Test Specimen 1 after Thermal Loading..... | 57 |

| | |
|---|----|
| Figure A2: ϵ_{yy} Strain Map of Test Specimen 1 after Thermal Loading..... | 57 |
| Figure A3: ϵ_{xx} Strain Map of Test Specimen 2 after Thermal Loading..... | 58 |
| Figure A4: ϵ_{yy} Strain Map of Test Specimen 2 after Thermal Loading..... | 58 |

List of Tables

| | |
|---|----|
| Table 1: ASTM Thermocouple Types | 12 |
| Table 2: AL 6061-T6 Mechanical Properties | 14 |
| Table 3: Test Matrix | 20 |
| Table 4: Nusselt Number Distribution | 26 |
| Table 6: Unperturbed Variable Values..... | 49 |

Nomenclature

| | | |
|------------|---|--------------------------------------|
| q'' | = | heat flux |
| h | = | convection heat transfer coefficient |
| T_s | = | surface temperature |
| T_∞ | = | free stream temperature |
| k | = | thermal conductivity |
| ΔT | = | temperature difference |
| L_c | = | characteristic length |
| ϵ | = | emmissivity |
| σ | = | Stefan Boltzman Constant |
| T_{surr} | = | temperature of surroundings |
| Bi | = | Biot number |
| T_i | = | initial temperature of lumped mass |
| A_s | = | surface area |
| ρ | = | material density of lumped mass |
| V | = | volume of lumped mass |
| c | = | specific heat of lumped mass |
| D_j | = | nozzle exit diameter |
| E | = | modulus of elasticity |
| ν | = | Poisson's ratio |
| α | = | linear thermal expansion coefficient |
| r | = | radius of impingement zone |
| b | = | plate thickness |
| s | = | steel plate |
| M | = | Mach number |
| T_0 | = | total temperature |
| p_0 | = | total pressure |

Nu = Nusselt number

rad = radiation

$conv$ = convection

1. Introduction

1.1 Background & Motivation

Throughout the history of the United States Navy, steel has been the preferred material choice for the construction of ship hulls and structures. However, various alternative materials, such as aluminum and other alloys, have been considered over the years in an effort to reduce some of the disadvantages of building with steel. Aluminum alloys in particular have been utilized for their ability to retain structural strength while reducing weight by up to 50%, when appropriately designed [1]. For this reason, various ship structures composed of aluminum alloy have appeared in naval vessels since the 1890's. Beginning in the post-World War II era, the U.S. Navy began designing ship superstructures of aluminum alloy [2]. This design not only reduced overall ship weight, but shifted the vertical center of gravity towards the keel, resulting in better transverse stability [3]. Ships with this superstructure design included the Ticonderoga-class guided missile frigates and Oliver Perry-class frigates, both of which sustained severe cracking while deployed [4]. Furthermore, it was recognized that aluminum begins to lose strength at less than a third of the temperature at which steel begins to lose strength. As such, aluminum performs poorly in comparison to steel under application of fire, which a naval ship must be prepared to sustain under attack [1, 2]. Ultimately, the high maintenance costs required to repair the aluminum superstructures drove the leadership of the U.S. Navy to move back to steel construction by the early 1990's [1].

Although the U.S. Navy continued to construct smaller vessels of aluminum alloy in the interim, the material was not used in larger scale ship construction until the early 2000's. Of primary interest are the new Littoral Combat Ships (LCS) and Joint High Speed Vessels (JHSV). There are two lines of LCS, one produced by Lockheed Martin Corporation and the other produced by Austal. The Lockheed Martin line has a steel hull and aluminum superstructure construction, whereas the Austal line is built with an aluminum hull. The JHSV line, manufactured by Austal, also features an aluminum hull.

These ships were designed to support helicopter operations, but were not initially intended to support the landing of other aircraft. Space constraints restrict runway take-off and landing operations, such that only vertical operations could be supported. Additionally, the aluminum decks were not designed to withstand the thermal loads generated by other Vertical Take-off and Landing (VTOL) aircraft. As this type of aircraft prepares for landing or take-off, the engine exhaust plumes are pointed in the direction of the ship flight deck, subjecting the deck to high temperatures. Although the LCS and the JHSV ships were not designed to support the landing and associated thermal loads of VTOL aircraft, it may prove economically and strategically advantageous to investigate the potential capability of these ships in such operations.

The Boeing V-22 Osprey is an example of such a VTOL aircraft with thermal loads on the lower range of the spectrum in comparison to other VTOL aircraft, such as the F-35B [11]. Since there is a greater chance that any flight deck would be able to support a lower thermal load than a higher thermal load, this study will focus on the application of thermal loads similar to those nominally produced by the V-22.

Heat transfer through the flight deck may have adverse effects on the other aluminum components of the ship. Therefore, the behavior of the heat transfer through the deck must be taken in to consideration. Furthermore, the aluminum alloy decks panels on these modern ships are designed with a corrugated middle section sandwiched between two nominally flat plates. This design, conceptually similar to that of LASCOR – a corrugated steel design – increases the strength of the panel [5]. An example of a corrugated aluminum alloy panel cross-section may be seen in Figure 1. The presence of the corrugation layer in these deck panels is expected to add an element of complexity the heat transfer through the panel as compared to that of a flat plate. This study seeks to clarify the effects of applying thermal loads generated by a heated, circular, subsonic jet impinging on sections of aluminum alloy corrugated ship deck panel by examining:

- 1) the heat transfer coefficient distribution on the upper surface of such panel sections,
- 2) qualitative infrared images revealing thermal paths through ship deck panels
- 3) the effects of the variable geometry of corrugation on heat transfer through

aluminum alloy deck panels under these loads.

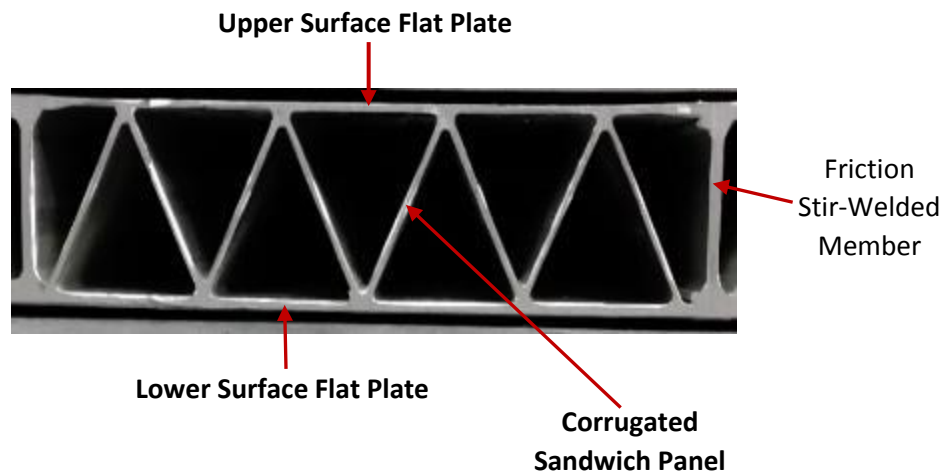


Figure 1: Cross-section of an Aluminum Alloy Ship Deck Panel

1.2 Overview

Aluminum ship deck panels, such as shown in Figure 1, are the focus of this study. The behavior of the heat transfer through these corrugated panels may be investigated by three methods: quantitatively via collection transient thermocouple data, qualitatively via infrared imaging, and theoretically based on a thermal resistance model.

Thermocouple data was taken on the surface of the panel opposite to the surface on which thermal loads were applied. Thermocouples attached at the same locations on varying specimen may be compared to reveal the effects of panel geometry variations on heat transfer.

The heat transfer both through thickness and across the surface of the panel to which heat is applied may be qualitatively evaluated via thermal imaging with infrared cameras. These images highlight the path of heat transfer along the surface which is captured in the photograph. It is expected that points of contact where the corrugation is welded to the flat plate surfaces of the panels will provide dominant heat transfer paths outward from the region to which heat is applied.

Finally, a thermal resistance model, based on an analogy to electrical circuit analysis was developed for the cross-section of each deck panel specimen studied. This results of these models indicate the primary pathways for heat transfer from points of interest from one surface of a panel through to the other (upper or lower).

2. Problem Description and Review of Relevant Literature

2.1 Review of Subsonic Impinging Jet Characteristics and Zones

The pertinent regions of a subsonic jet impinging on a flat surface are the similar to those of a free jet with the additions of what may be called the impingement zone and a wall jet zone. These regions are qualitatively designated in Figure 2 below. The length of the potential core extends may be quantified in terms of nozzle exit diameters downstream of the nozzle exit plane and depends on the nozzle exit Reynolds number. The shear layer, surrounding the potential core in the free jet zone, and the wall jet zone exhibit turbulent behavior [6]. For this reason, jet testing which calls for laminar flow conditions is typically conducted within the region of the potential core.

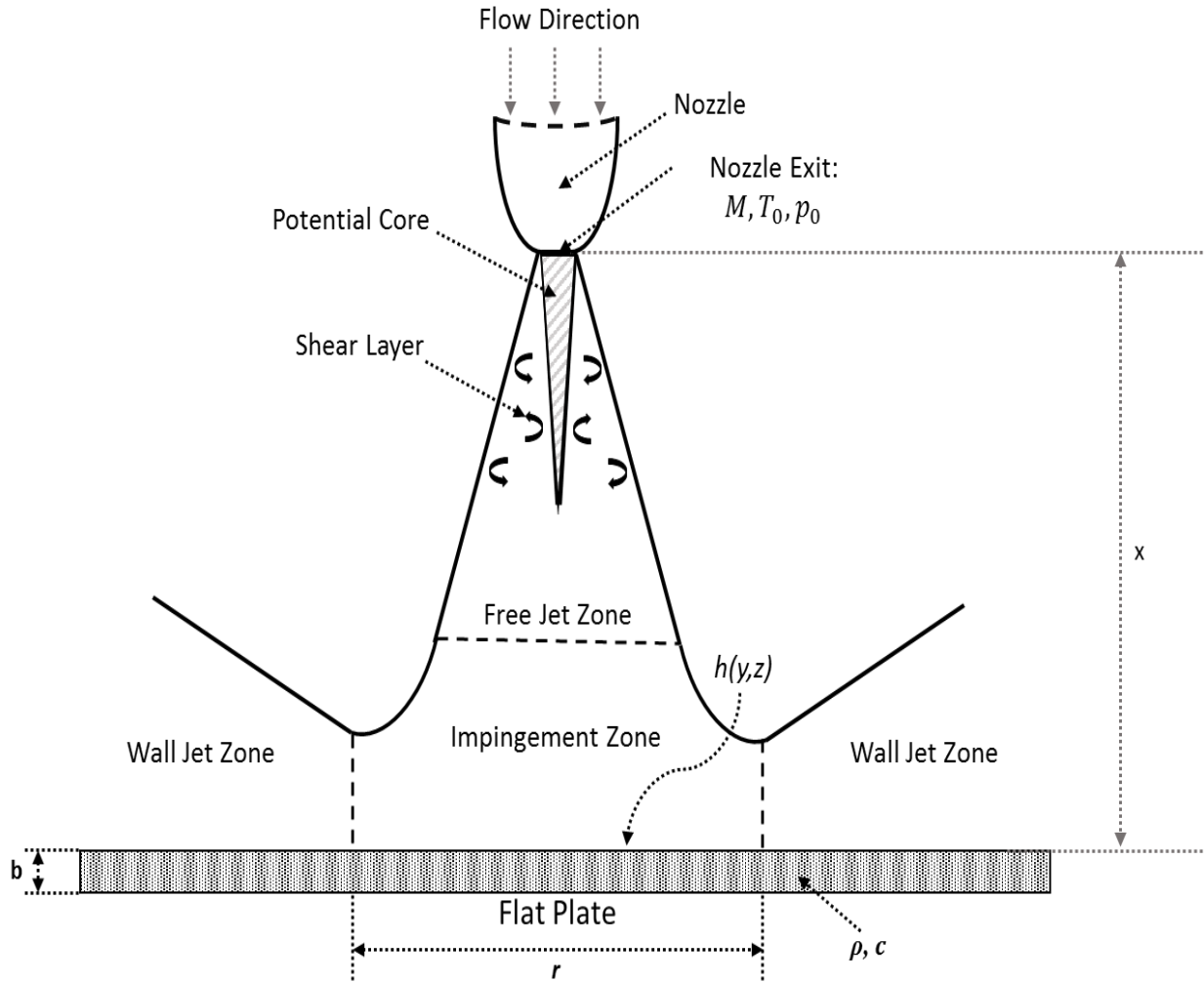


Figure 2: Schematic of a Subsonic Circular Jet Impinging on a Flat Surface [6]

2.2 Heat Transfer Fundamentals

In order to fully understand the behavior of any heat transfer phenomenon, it is critical to first understand the driving methods by which heat transfer occurs. There are three fundamental modes of heat transfer: conduction, convection, and radiation. Depending on the application, it is likely that one or two of these modes will play a dominant role. Each of these modes may be analytically quantified by their respective heat transfer rate per unit area, or heat flux, through the medium in question [7].

2.2.1 Heat Transfer Modes: Convection, Conduction, & Radiation

The convection heat transfer mode applies specifically to heat transfer through fluid mediums into solid mediums. This mode essentially propagates heat via the mixing of fluid regions on both molecular and large scales. The heat flux for convection heat transfer is defined in Equation 1 below [8].

$$q'' = h(T_s - T_\infty) \quad (1)$$

Equation 1 introduces the convection coefficient to be discussed in a following section.

The conduction heat transfer mode, unlike convection, can occur through either fluid or solid mediums. Rather than transferring energy via motion of fluid particles, the conductive exchange of energy occurs on a molecular level. Transfer of energy in the form of heat flows from more energetic to less energetic molecules via translational, vibrational, and rotational molecular excitement. The heat flux due to conduction is defined below in Equation 2 as a function of the thermal conductivity of the medium, the temperature differential across the medium, and the physical dimension of the medium in length [7].

$$q''_{cond} = k \frac{\Delta T}{L} \quad (2)$$

Finally, heat may also be transferred via radiation. This heat transfer mode, unlike the previous two, does not require a medium through which the energy is transmitted. Rather it is transferred via electromagnetic waves from one material to another. This means radiation can occur across a vacuum. For clarity, this is the mode by which the sun heats the earth. Heat flux due to radiation may be analytically defined as a function of the temperature differential between a surface in question and its surroundings and the emissivity of the surface to which heat is transferred [7]. Further description of emissivity is beyond the scope of this work. The relation for radiative heat flux is given below in Equation 3.

$$q''_{rad} = \epsilon \sigma (T_s^4 - T_{surr}^4) \quad (3)$$

2.2.2 Convection Heat Transfer Coefficient

This work is focused on mimicking the heat transfer from the exhaust core of a VTOL aircraft onto aluminum alloy corrugated ship deck panels. Since heat is transferring from the exhaust, which is fluid in large scale motion, onto the surface of the panels, the primary component of heat transfer seen in this work is due to convection. Furthermore, the exhaust thermal loads will be partially defined by the application of a convection heat transfer coefficient distribution onto the panel surfaces, as will be discussed in more detail in subsequent sections. It is therefore important to develop an understanding of the convection heat transfer coefficient, first shown in Equation 1. This term is dependent on the development of the boundary layer on the surface to which heat is transferred during a convection heat transfer phenomenon. In this work, values of convection heat transfer coefficient will be determined experimentally and matched via successive testing to a desired coefficient distribution similar to that of the nominal V-22 exhaust plume core, as provided for public distribution in reference 11.

2.2.3 Nusselt number

The Nusselt number is a key parameter in non-dimensionalizing heat transfer. It is analytically described by the Equation 4.

$$Nu = \frac{h L_c}{k_s} \quad (4)$$

Additionally, Nusselt number in a conceptual sense is defined as the ratio of convective heat transfer to conductive heat transfer across the boundary of a thermal interface [7]. In the scenario of an impinging jet transferring heat to a flat plate, the Nusselt number gives the ratio of convective to conductive heat transfer from the fluid in the impingement zone to the material of the plate. In the case of a jet, the characteristic length is the jet diameter, D_j .

2.2.4 Reynolds number

Reynolds number is also a dimensionless parameter that is key to parameterizing any given flow. This dimensionless parameter is a ratio of inertial forces of the flow to the associated viscous forces and is analytically defined in Equation 5. Reynolds number is critical for purposes of comparing data from various studies and for the purposes of repeating tests under varying dimensional flow conditions

$$Re = \frac{V D_j}{\nu} \quad (5)$$

2.2.5 Lumped Capacitance Method

The Lumped Capacitance Method is a simple theoretical method for predicting the transient temperature of a solid experiencing conductive heat transfer. The main underlying assumption of this method is that the solid to which heat is transferred maintains a uniform temperature throughout during the period of time over which the temperature of the solid continues to change. This assumption may be considered valid for scenarios in which Biot number, to be discussed in the following section, is lower than 0.1 ($Bi \ll 1$). This period of time extends until the solid and the fluid to which it is subject reach equilibrium, such that the temperature of the solid is T_∞ [7]. According to this theoretical model, the transient temperature of the solid in question is a function of its initial temperature, the temperature of the flow, the convection heat transfer coefficient, time, and several material properties and physical dimensions of the solid itself. Equation 6 below provides the analytical expression of the Lumped Capacitance Method model.

$$T = (T_i - T_\infty)e^{-\left(\frac{h}{\rho bc}\right)t} + T_\infty \quad (6)$$

It is often preferential to use dimensionless parameters to describe flow conditions. These parameters are typically more relatable for readers and those wishing to replicate any stated

work [9]. For this purpose, Equation 6 may be re-organized in terms of several known dimensionless terms including a dimensionless temperature, Biot number, and Fourier number as shown below in Equation 7.

$$\theta^* = e^{-Bi*Fo} \quad (7)$$

2.2.6 Biot Number

One of dimensionless parameters pertinent to the description of flow fields and to the application of the Lumped Capacitance Method is the Biot Number. Conceptually, the Biot Number is a relation of the thermal resistances within the boundary layer on a surface and within the surface itself [7]. This parameter is a function of the convection heat transfer coefficient of the flow, the thermal conductivity of the surface material, and the physical dimension of the surface described as length. (Note that this surface is the face of a solid.) The analytical definition of Biot Number is given in Equation 8 below [7].

$$Bi = \frac{hL_c}{k} \quad (8)$$

2.2.7 Fourier Number

The next dimensionless parameter of interest is the Fourier number, which is a dimensionless measure of time. This parameter relates the rate of heat transfer via conduction through a solid object to the rate at which the object stores heat energy. A larger Fourier number indicates that the object conducts heat energy at a relatively greater rate, whereas a smaller value indicates the object stores energy at a relatively greater rate. The analytical definition of the Fourier number is given below in Equation 9.

$$Fo = \frac{kt}{\rho c L_c^2} \quad (9)$$

2.2.8 Dimensionless Temperature

Finally, the temperature may also be rearranged into a ratio of temperature differences, such that it is dimensionless. The difference in transient plate temperature and freestream temperature may be defined as θ and the difference in initial plate and freestream temperature may be defined as θ_i (Eqs. 10 & 11).

$$\theta = T - T_\infty \quad (10)$$

$$\theta_i = T_i - T_\infty \quad (11)$$

The ratio of these two differences may then be defined as the dimensionless time parameter as in Equation 12.

$$\theta^* = \frac{\theta}{\theta_i} \quad (12)$$

2.3 Thermal Loads Generated by VTOL Operations

This study focuses on thermal loads mimicking those generated during VTOL operations such as those produced by the V-22. As previously mentioned, the nominal thermal loads generated by this aircraft are available for public distribution in reference 11. These loads are defined by the distribution of temperature and convection coefficient that the aircraft's exhaust plume applies to the surface on which it is landing. The nominal, radially symmetric profiles of the stagnation temperature and convection heat transfer coefficient distributions on the landing surface are presented visually in Figures 3 & 4 below [11].

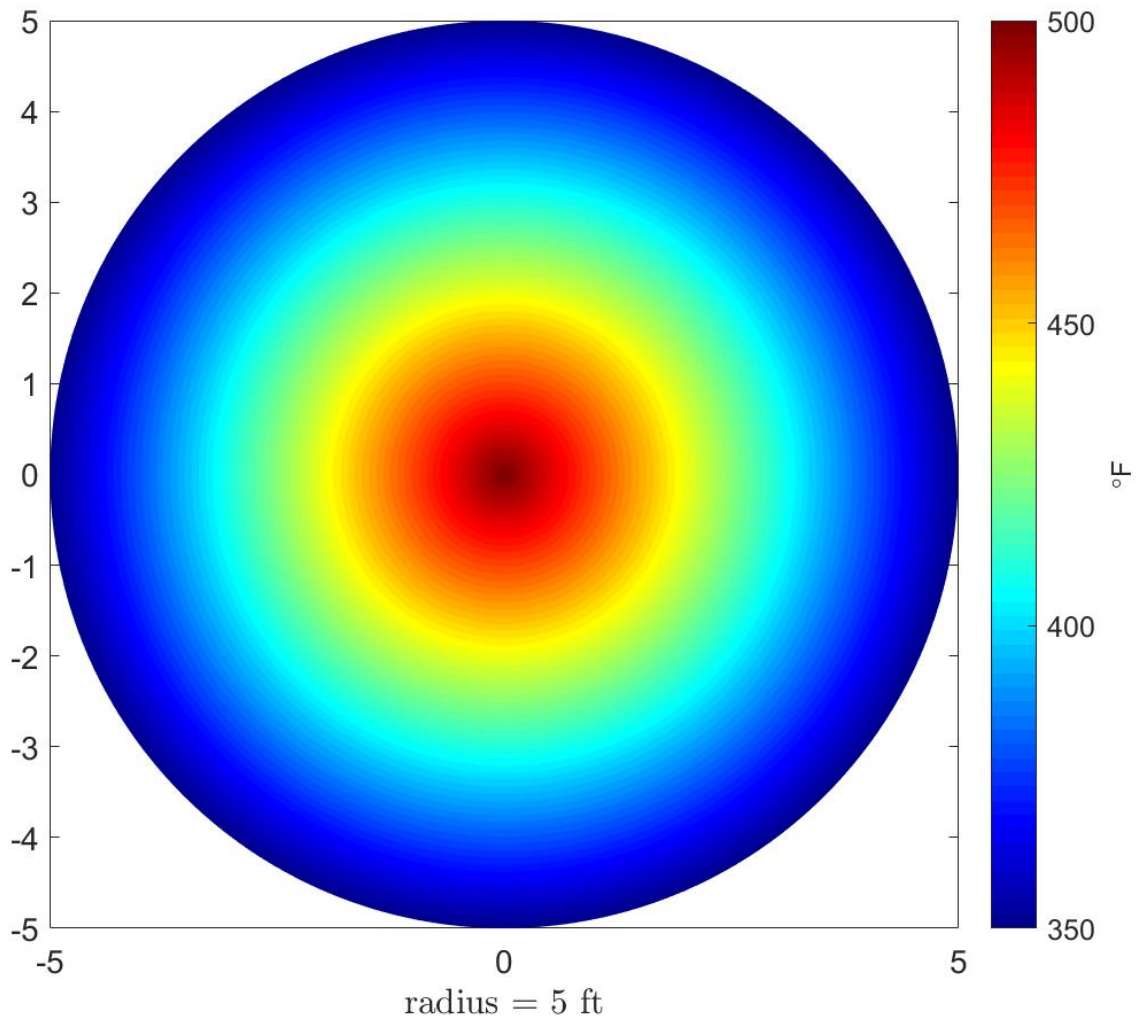


Figure 3: Nominal V-22 Osprey Stagnation Temperature Profile on Landing Surface [11]

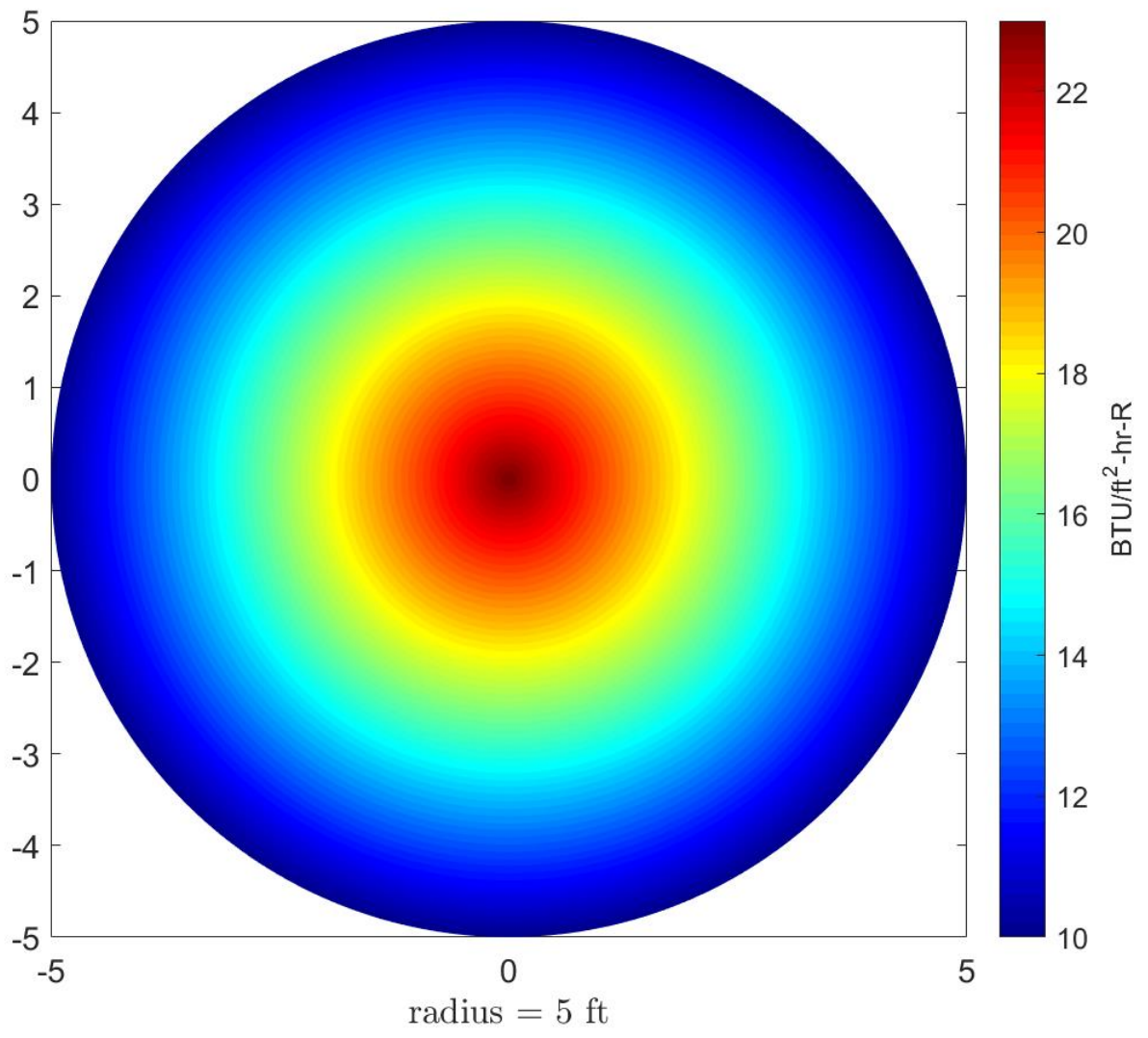


Figure 4: Nominal V-22 Osprey Convection Coefficient Profile on Landing Surface [11]

3. Experimental Approach

3.1 Surface Thermocouples

A thermocouple is defined as wires of two dissimilar metals joined together at two junctions. The temperature at one junction is known and is used as a reference temperature, while the temperature at the other junction is unknown. Each metal has an inherent thermal resistivity different from its counterpart. Due to this difference in resistivity, the difference in temperature at these two junctions generates a voltage through the wires. The difference in voltage between the two junctions may be translated into a difference in temperature if the thermocouple is properly calibrated such that units of voltage correspond to units of temperature. The correspondence of voltage to temperature difference is known as the Seebeck effect. The initially unknown temperature is determined based on this difference in temperature and the reference temperature at the other junction [12].

3.1.1 Thermocouple Configurations & Types

Thermocouples come in a large range of variety depending on the types of dissimilar metals used and the configuration of the unknown temperature junction. Two of the most basic thermocouple configurations are bare wire and sheathed [10]. A bare wire thermocouple simply means that the measurement junction – where the temperature is considered unknown – is exposed directly to the medium that it is measuring. The measurement junction of a sheathed thermocouple however, is fully encapsulated in some other material. Sheathed thermocouple are typically comprised of an insulating material directly in contact with the thermocouple wires near to the measurement junction, which is then encased in another metallic material [12].

As mentioned, thermocouples are further classified by the types of dissimilar metals of which they are composed. There are 9 existing ASTM-recognized thermocouple types, based on their composition: types J, K, T, N, E, C, R, S, and B [12]. Each is best suited to certain conditions and temperature ranges based on the reaction the corresponding metals to different types of environments. A list of thermocouple the most common thermocouple types, their metallic compositions, and appropriate temperature ranges is given in Table 1 [13].

Table 1: ASTM Thermocouple Types

| Type | Wire Composition | Temperature Range (°F) |
|----------|--|------------------------|
| J | Iron & Constantan | 32 – 1400 |
| K | Chromel & Alumel | -328 – 2300 |
| T | Copper & Constantan | -328 – 698 |
| N | Nicrosil & Nisil | -328 – 2300 |
| E | Chromel & Constantan | -328 – 1652 |
| R | Platinum Rhodium-13% & Platinum | 32 – 2696 |
| S | Platinum Rhodium-10% & Platinum | 32 – 2696 |
| B | Platinum Rhodium-30% & Platinum Rhodium-6% | 1598 – 3092 |

3.1.2 Contact Resistance

On a very small scale, the interface between each surface will consist of a collection of minute points of true contact. The smoother each surface is, the more contact points there will be at their interface. Since the bead of a bare wire is very significantly smaller than that of a flat-sheathed thermocouple, there will be significantly fewer contact points at that interface with a surface than that at the latter. Each contact point provides a thermal path for heat transfer. It follows, then that the fewer thermal paths existing at a given interface, the greater the thermal resistance will be between the surfaces in contact [14]. Furthermore, the expected range of temperature measurements necessary for this work was approximately 15° - 260°C. Therefore, in order to reduce this contact resistance, a flat-sheathed, Type K surface thermocouple was found to be most suitable for taking the surface temperature measurements in this work.

3.2 Aluminum Alloy Deck Panel Description

The testing detailed in this work was conducted using two configurations of aluminum alloy corrugated ship deck panels as test specimen. These panels have a design similar to that of the flight decks of the U.S. Navy’s modern aluminum-hulled ships, as detailed in §1.1. These panels are essentially comprised of two flat plates sandwiched around a layer of corrugation. Each panel is connected to the next panel by a vertical member of the corrugation which is Friction Stir-Welded onto the next panel. The two specimen tested in this work are both composed of a total of two panels connected together (Figure 1). For the purpose of evaluating the effects of the Friction Stir-Welds (FSWs) on the material, one specimen is configured such that this member is along the centerline of the panel, as shown in Figure 5. The second test specimen is configured such that the center is one full panel with an additional half panel connected on either edge of the central panel. In this configuration, the centerline of the panel runs halfway between two symmetric FSWs, as indicated in Figure 6.

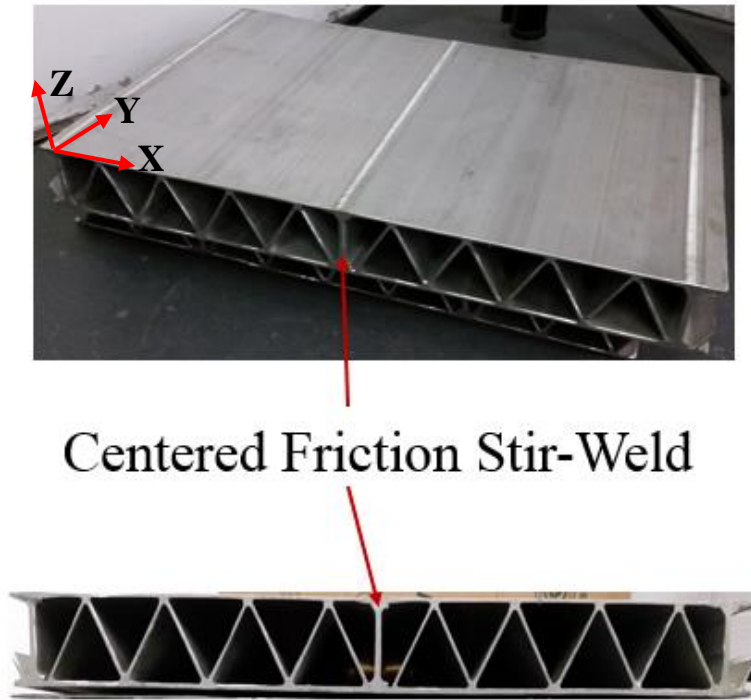


Figure 5: Test Specimen 1. FSW member is along centerline of cross-section

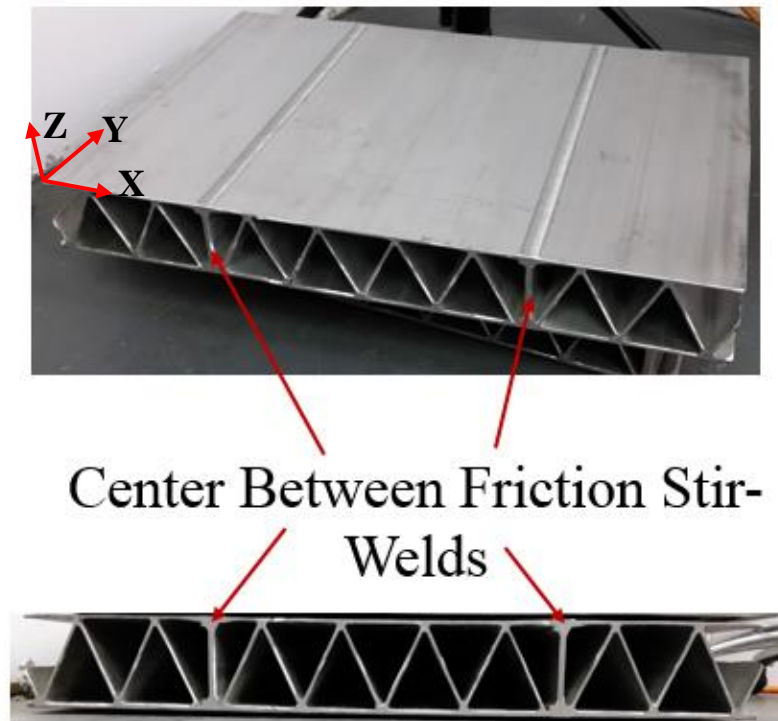


Figure 6: Test Specimen 2. FSW members symmetric about centerline of cross-section

Both specimen have an approximate length of 30” in the x-direction, a width of 19.50” in the y-direction. The coordinate systems for these coordinate systems are indicated in Figures 5 & 6. Each specimen is comprised of the aluminum alloy AL-6061. Material properties of AL-6061 at approximately 500°F are given below in Table 2 [15, 16, 17].

Table 2: AL 6061-T6 Mechanical Properties

| Yield Strength (psi) | Coefficient of Thermal Expansion ($\mu\text{in /in-}^\circ\text{F}$) | Thermal Conductivity (BTU/hr-ft- $^\circ\text{F}$) | Elastic Modulus (ksi) | Poisson's Ratio |
|----------------------|--|---|-----------------------|-----------------|
| 4930 | 14.0 | 107 | 7850 | 0.33 |

During testing all faces and edges of each specimen were insulated with a 1” thick ceramic blanket insulation, to prevent heat transfer due to the surroundings.

3.3 Virginia Tech Hot Jet Facility

The Virginia Tech Hot Jet was used in this study for the purpose of replicating the core of the V-22 Osprey exhaust plume. The jet is located at the Virginia Tech Advanced Propulsion and Power Lab in Blacksburg, VA. The jet is driven by compressed air fed from a Boge S341 air compressor capable of compressing air up to 180 psig and achieving a continuous flow rate of 3.5 lbm/s [18]. The air issuing from the compressor is then dried before entering a Sylvania 192 kW Flanged Inline Heater (Model 073153). Downstream of the heater, the jet contracts from 8” to a 4” section, where it is passed through a series of three stainless steel mesh screens and a 2” thick segment of 16 CPSI honeycomb to condition the flow. Total temperature and pressure may be measured in this section by inserting a bare wire (Type K) thermocouple and a Pitot probe into small openings in the wall of the jet. The facility may be run continuously over a Mach range of approximately 0.15 – 2, depending on an interchangeable nozzle configuration [19]. For the purpose of this study, a 2” subsonic nozzle was used and the jet was run over a Mach range between 0.21 and 0.32. Additionally, the jet plenum total temperature for this work was approximately 805°F. Based on the method presented by Witze, the potential core of the jet under these conditions is approximately 3 D in length downstream of the nozzle exit [20]. A picture of the jet may be seen in Figure 7, and a schematic indicating the discussed components may be seen in Figure 8.



Figure 7: Image of Virginia Tech Hot Jet Facility at the Advanced Propulsion and Power Laboratory

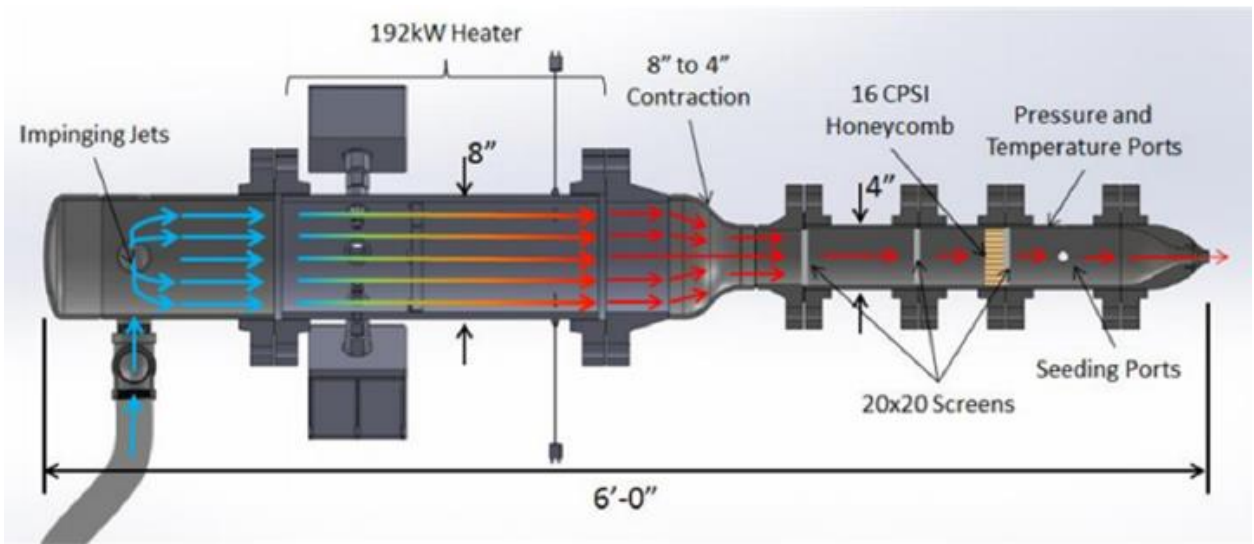


Figure 8: Schematic of Virginia Tech Hot Jet Facility

3.4 Experimental Specimen Mounting Rig

It is important to note that since the jet facility is oriented horizontally (perpendicular to the orientation in which the exhaust plume would emanate from a V-22), the specimen were mounted normal to their orientation on a ship. Therefore, what is called the upper surface of the specimen in their typical orientation, will now be referred to as the front surface; similarly, the lower surface will now be referred to as the back surface. A mount was designed to align each test specimen in a desired orientation with respect to the jet in a

manner which reduced internal stresses in the specimen as much as possible. This was achieved by hanging the specimen from the frame such that it was under tension. Additionally, to prevent movement in the z-direction (in specimen's coordinate system), pressure was applied on the back surface of the panel. Ultimately, this method of mounting the specimen in the jet stream restricted only three degrees of freedom – translational motion in all directions. The mount was then positioned such that the center of the upper surface of each specimen was aligned with the center of the jet nozzle and was located 5D downstream of the nozzle exit in the streamwise direction of the jet (Figure 9 & 10).

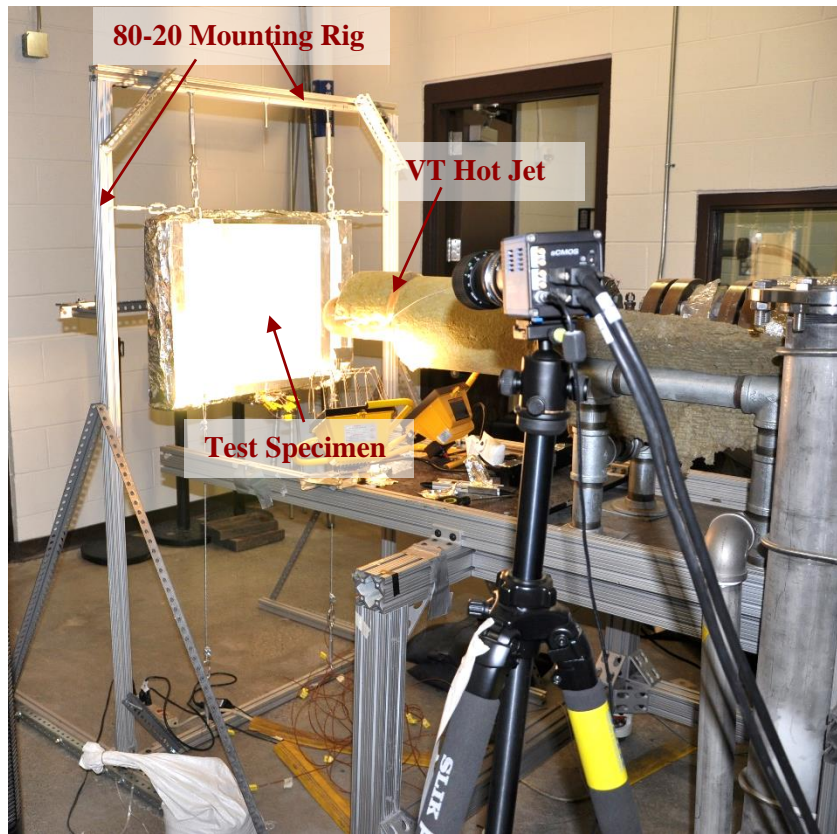


Figure 9: Test Specimen Positioned in Experimental Mounting Rig



Figure 10: Side View of Test Specimen Positioned in Experimental Mounting Rig

3.5 Instrumentation

Two methods of data collection were employed in this study. Temperature data was taken using surface thermocouples and infrared images.

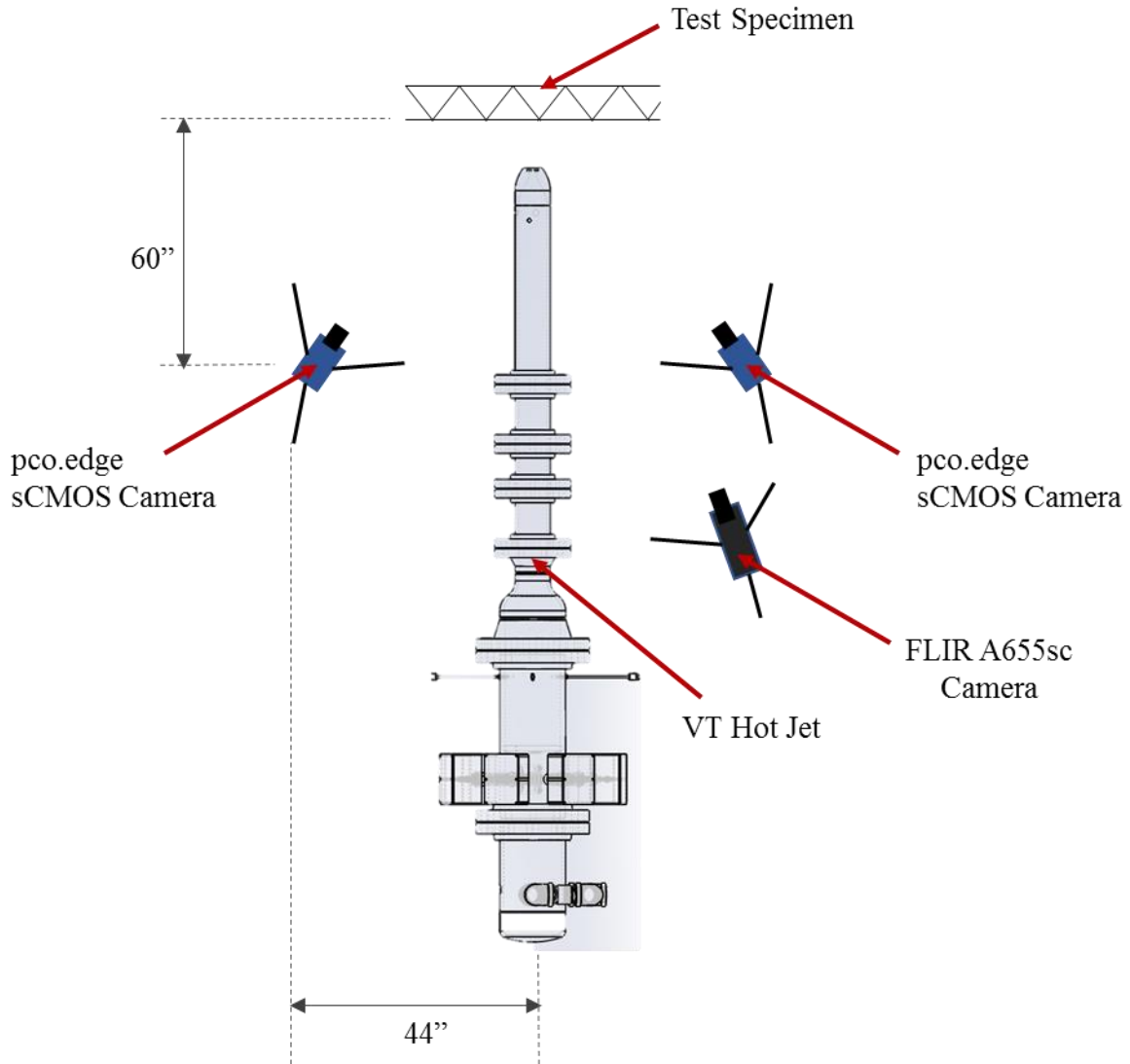


Figure Not to Scale

Figure 11: Overhead View of Equipment and Instrumentation Configuration

Infrared images were collected throughout the course of the tests in this study. These infrared images were taken with a FLIR A655sc thermal camera. Relative positioning of this camera is depicted in Figure 11. These images were taken purely for qualitative purposes, to provide an illustration of the qualitative temperature distribution applied to each test specimen during testing.

3.5.1 Temperature Probes

The surface thermocouples used in this work were Omega Type K Bolt-On Surface Thermocouples. These were adhered to the back surface of the each test specimen using Original Cold Weld Formula J-B Weld epoxy. The J-B Weld was applied such that no epoxy came between the thermocouple-specimen surface interface. Additionally, to reduce the contact resistance between the thermocouple and the specimen, a thin film of XSPC-K3 thermal paste was applied to each thermocouple just before application of the thermocouples to the specimen. Nine thermocouples in total were applied to the back surface of each specimen in the orientation depicted in Figure 12. These thermocouples span a field corresponding to the field of view of the front surface which was photographed for DIC analysis.

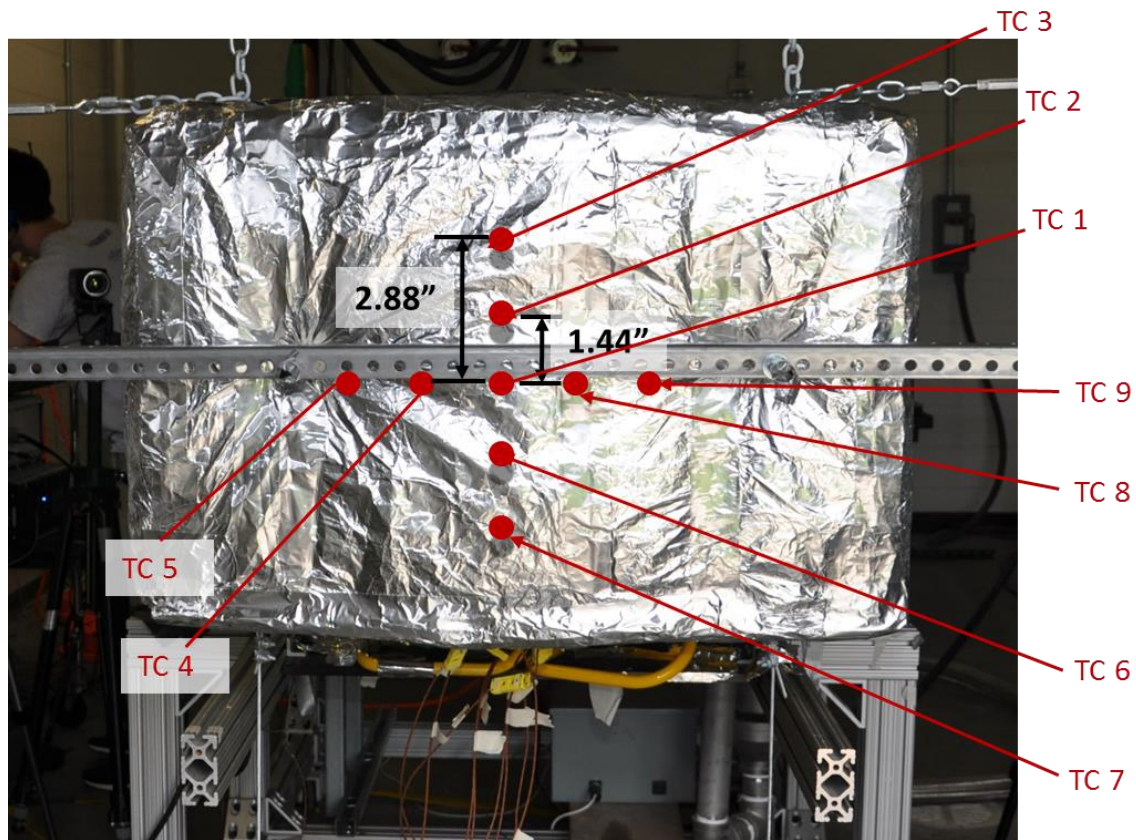


Figure 12: Back Surface Thermocouple Configuration Schematic

3.6 Experimental Procedures

Testing in this study was conducted in two phases. The purpose of Phase 1 was to determine the necessary jet facility settings to produce the desired thermal loading to match the core temperature values as defined in Figure 3. Testing for Phase 1 was conducted using a 23" x

23” x ¼” HSLA-100 steel plate. Steel was used for its lower thermal expansion coefficient as compared to aluminum. Therefore, repeated tests could be performed on the steel plate without risk of appreciable deformation. Phase 2 consisted of applying the facility settings learned during Phase 1 to the test specimen, such that thermal loads similar to those generated by the exhaust plume of an aircraft in VTOL operations were applied to front surface of each specimen. A complete test was defined by an hour of applied thermal loads followed by an hour of unforced cooling. A test matrix for each phase is given below in Table 4. The Biot number, which can only be directly calculated for Test #1, due to variable geometry in the other tests is 0.007. Because this value is lower than 0.1, the Lumped Capacitance Method is deemed a valid model for this test.

Table 3: Test Matrix

| Test Phase | Test # | Specimen | D_j (in) | T_{tj} (°F) | Mach number | Reynolds number | Plate Location |
|------------|--------|----------------------|------------|---------------|-------------|---------------------|----------------|
| 1 | 1 | HSLA-100 ¼” plate | 2 | 805 | 0.3 | 1.209×10^5 | 5D |
| 2 | 2 | Test Specimen 2 | 2 | 810 | 0.3 | 1.209×10^5 | 5D |
| 2 | 3 | Test Specimen 1 | 2 | 810 | 0.3 | 1.209×10^5 | 5D |

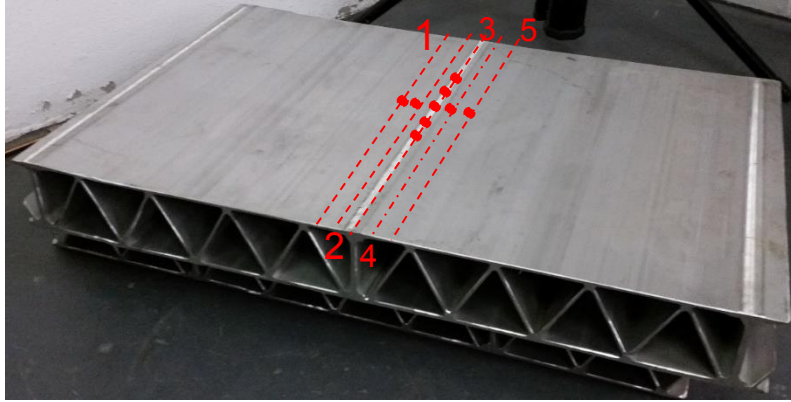
3.6.1 Testing Phase 1

During this phase, the pressure of the compressed air flowing through the jet, and the heater temperature settings were the two facility setting variables. Transient temperature data was taken on the back surface of the steel plate throughout the course of each test at 9 thermocouple locations as shown in Figure 12. The desired temperature curve versus time at each thermocouple location was defined based on a Lumped Capacitance Method for the steel plate and the core temperature from Figure 3. This approach based on the Lumped Capacitance Method was used by Maranzana *et al* in Reference 21. Numerous other studies have also taken an approach based on this method [21 - 27]. The experimental transient temperature data on the center of the back surface of the steel plate was then plotted against theoretical curves, which are dependent on both front surface jet temperature and convection heat transfer coefficient. Jet pressure (which may be translated to jet Mach number) and heater temperature was varied over the course of multiple tests until the experimental curve was found to closely match the theoretical curve. The test which yielded results with the closest match was then repeated several days later to confirm repeatability. The convection heat transfer coefficient at each thermocouple location was determined from those values used to calculate each of the matched theoretical temperature curves corresponding to each thermocouple. Note that this approach of comparing data to theory based on the Lumped Capacitance Method was only used in this phase of testing (with a solid plate specimen) in

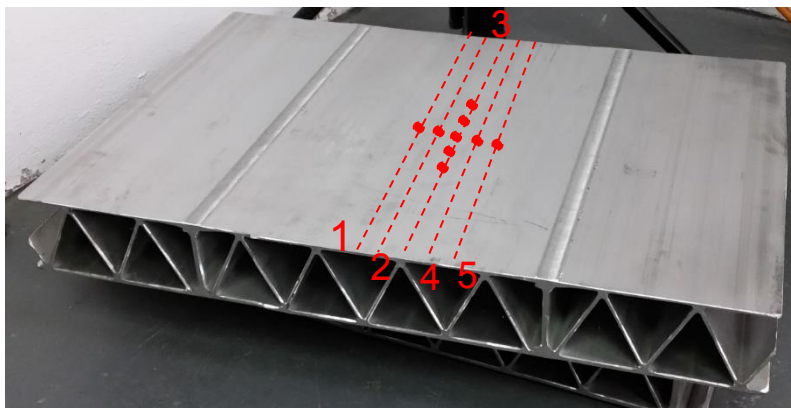
order to determine the jet settings necessary to generate the desired thermal loads. Lumped Capacitance Method was not used in the following testing phase.

3.6.2 Testing Phase 2

Using the appropriate jet facility Mach number and temperature settings determined in Phase 1, the thermal loads in terms of front surface temperature and convection coefficient distribution – as determined from Phase 1— were then applied to each test specimen during two separate tests. The key parameters for these tests are also given in Table 4. Each specimen was loaded for 1 hour, after which the jet was shut down as data was continuously collected for an additional hour. During this second hour, the specimen experienced unforced cooling. Infrared images were collected at consistent intervals during the first hour of the test. Additionally, transient temperature data was collected at 9 points on the back surface from thermocouples as detailed in §3.6.2. Although the thermocouples were positioned on both specimen in the arrangement shown in Figure 12, it is important to note that the positioning of the corrugation in the sandwich layer lines up with the centerline of the specimen differently. For Test Specimen 1, the FSW member lies directly along the centerline of the specimen. However, for Test Specimen 2, along the back surface, a typical weld line lines up directly with the centerline of the specimen. Figure 13 below qualitatively show the locations of the thermocouples in relation to the weld lines of the corrugation. The red points indicate the thermocouple locations and the dotted red lines highlight their locations relative to the weld lines along the back surface of the panel. The geometry of a cross-section of each specimen taken along each of these dotted lines will be the same along the length of the plate. Therefore, in future sections, these lines will be referred to as lines of constant geometry. Note that for each specimen thermocouples 1, 2, 3, 6, and 7 lie along the same line of constant geometry. Since the specimen are both symmetrical about the centerline, the geometry of the cross-section of the specimen will also be the same along lines 2&4 and 1&5. Therefore the thermocouples lying on these lines of similar geometry may also be grouped together for comparison in later sections.



(a)



(b)

Figure 13: Back Surface Thermocouple Configuration in Relation to Weld Lines for (a) Test Specimen 1 and (b) Test Specimen 2; spacing is not to scale – proper spacing is shown in Figure 12

3.7 Testing Lessons Learned

Because many aspects of the testing outlined above was relatively new to the author, many valuable lessons were learned. Firstly, after the first test specimen in Phase 2 was tested, it was found that the final segment of the jet facility, beyond the 8" to 4" contraction was set crooked to the axis of the rest of the jet such that the center of the jet nozzle exit was approximately 0.5" offset from the originally believed center. Since the final segment of the jet was slightly angled to the left (when facing downstream), that offset is only exacerbated with distance downstream of the nozzle exit. At 5D downstream, where each specimen was set, the offset of the specimen center from the jet center was significant enough that the region of the jet impinging on the center of the plate was approximate $130^{\circ}F$ less than that at the true jet center. This and any other unexpected qualities of the jet flow can be easily identified by characterizing the jet flow at the testing plane prior to testing.

Additionally, most of the thermocouples on the aluminum test specimen popped off at some point during testing. This is due to oxidation of most paints, coatings, etc. applied to aluminum materials. In this study, epoxy was used to attach surface thermocouples to the specimen surfaces. To avoid this issue, this method of attachment could have first been tested with small samples of aluminum material exposed to heat application. In keeping with the concept of this lesson learned, it is generally good practice to try any new testing method with a very simplified version of the final test.

Ultimately, these two primary lessons of

- 1) characterizing the testing plane and
- 2) trying very simplified experiments to evaluate method effectiveness prior to the main test,

are very broad and applicable to a wide range of testing types. These are both important lessons to take forward with all future testing.

4. Results & Discussion

The tests conducted in this study yielded two different categories of results: quantitative temperature via thermocouples and qualitative temperature via infrared imaging. Phase 1 results are purely based on thermocouple temperature data, while Phase 2 combines both result categories.

4.1 Phase 1 Test Results

The transient temperature data curve from the back surface of the steel plate is plotted against the theoretical transient temperature curve based on the Lumped Capacitance Method in Figure 14. The transient temperature data curve from a repeated test as detailed in §3.5.1 is also plotted in this figure. The jet facility was set to a heated Mach number of 0.30 and a plenum total temperature of 805°F to produce these results. Emphasis was placed on best matching the theoretical curves and the data curves in the initial 5 minutes of testing, as this transient portion of the curve defines the convection heat transfer coefficient. The convection heat transfer coefficient used to generate the theoretical curve indicates the value of that coefficient at the front surface of the steel plate corresponding to the location of the thermocouple. This procedure was followed for each of the 9 thermocouples on the back surface of the steel plate. A natural interpolation was then used to generate a full field of convection heat transfer coefficients within the region outlined by the thermocouples. This distribution may be seen in Figure 15. The corresponding Nusselt number at each thermocouple location on the steel plate is also listed in Table 5. Additionally, the Nusselt number distribution on the front surface of the steel plate as determined by a natural interpolation is given in Figure 16. The resulting Nusselt number at the stagnation point (approximately the location of thermocouple 1) is congruent with the stagnation point Nusselt number results determined by Jambunathan *et al* for an impinging heated circular jets at the Reynolds number of this study [28].

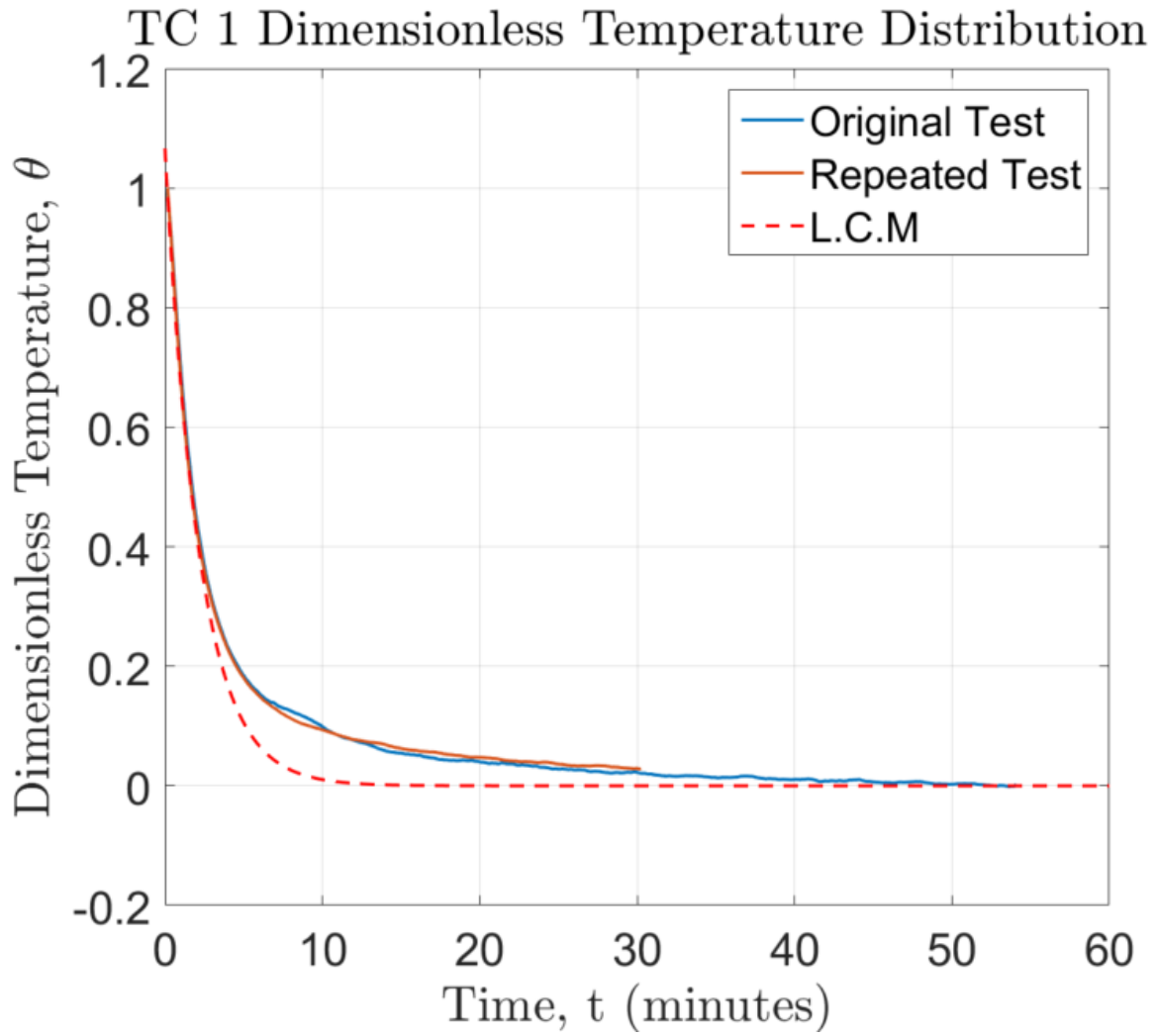


Figure 14: Phase 1 TC 1 Test Results vs. Theoretical Curve

Convection Heat Transfer Distribution on Front Surface of Test Specimen

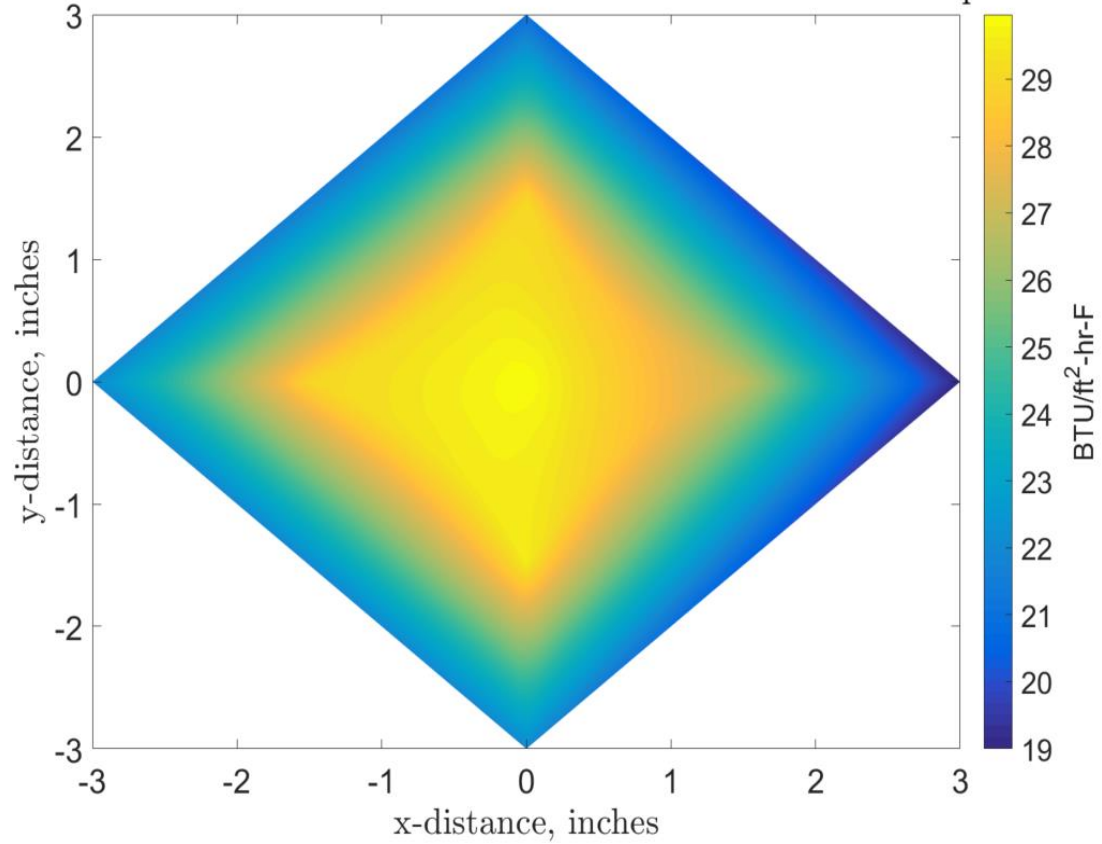


Figure 15: Convection Heat Transfer Coefficient Distribution on the Front Surface of the Steel Plate

Table 4: Nusselt Number Distribution

| | TC 1 | TC 2 | TC 3 | TC 4 | TC 5 | TC 6 | TC 7 | TC 8 | TC 9 |
|----|------|------|------|------|------|------|------|------|------|
| Nu | 203 | 196 | 142 | 183 | 129 | 200 | 149 | 196 | 149 |

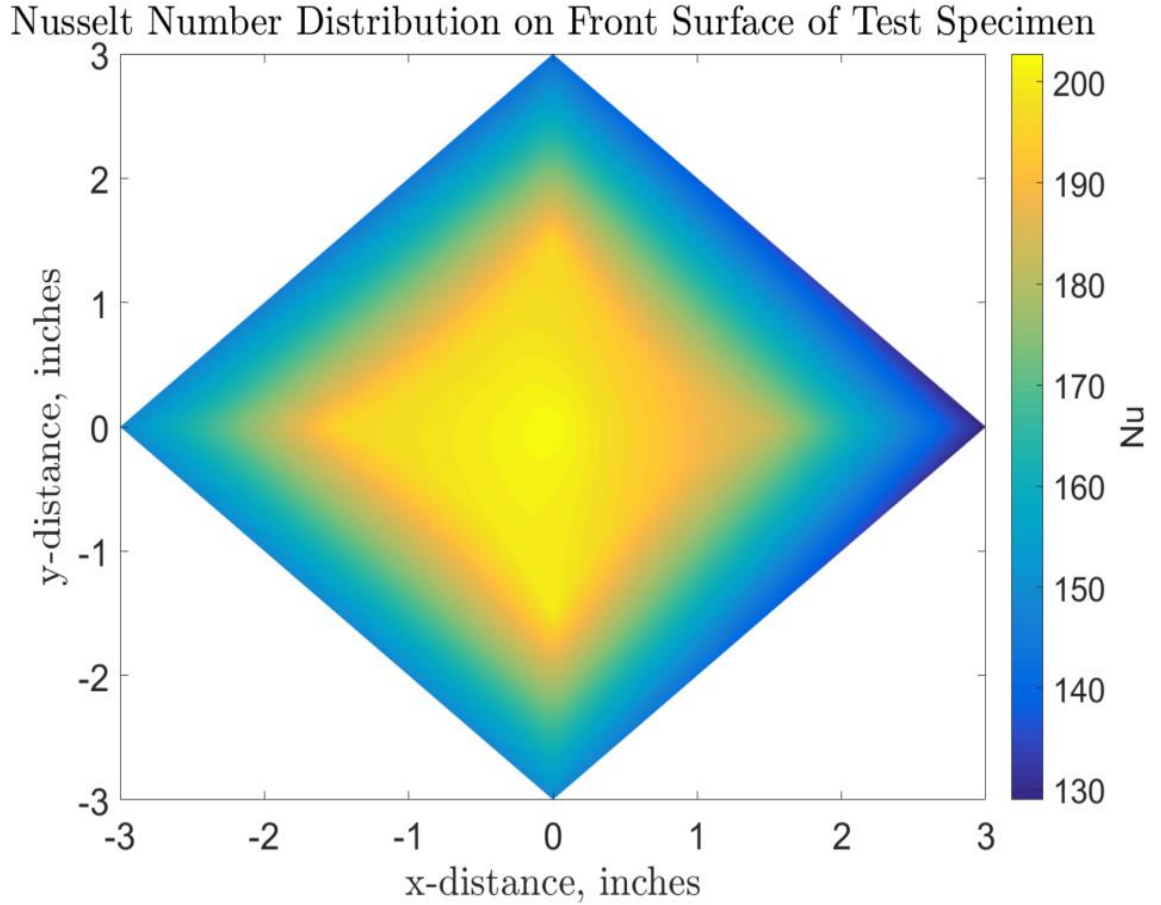


Figure 16: Convection Heat Transfer Coefficient Distribution on the Front Surface of the Steel Plate

Note that this study assumes that the primary mode of heat transfer from the jet into the specimen and heat transfer between the specimen and the surrounding air is convection. Radiation losses from the specimen to the surrounding environment were treated as negligible. This is confirmed by calculating the ratio of heat flux from radiation to heat flux from convection, $\frac{q''_{rad}}{q''_{conv}}$. Equations 13 and 14 below are used for the calculation of each heat flux in this ratio [7].

$$q''_{rad} = \sigma (T_{body}^4 - T_{surroundings}^4) \quad (13)$$

$$q''_{conv} = h (T_{body} - T_{fluid}) \quad (14)$$

In Equation 14, σ is the Stefan-Boltzmann constant. Based on these equations, the temperature of the steel plate and the stagnation temperature of the jet directly upstream of

the center of the plate, it was found that $\frac{q''_{rad}}{q''_{conv}} = 0.105$ in this test. Therefore, since the radiation losses are less than 11% of the convection heat transfer into the plate, convection dominates the results while radiation has an unmeasured, if much smaller, impact.

4.2 Phase 2 Test Results

4.2.1 Thermocouple Data

The transient temperature data curve from all of the 9 thermocouples on the back surface of Test Specimen 1 during the loading hour of test cycle is plotted in Figure 17. The transient temperature data curve from 5 of the 9 thermocouples on the back surface of Test Specimen 2 for the initial 30 minutes of the 2 hour test cycle is plotted in Figure 18. Data from the remaining 4 was not plotted because it was clear that they became disconnected during the test. Despite similarities to Figure 14, the results in Figures 17 and 18 were not used for thermal capacitance analysis based on a Lumped Capacitance Method due to the invalidity for the aluminum panel geometry.

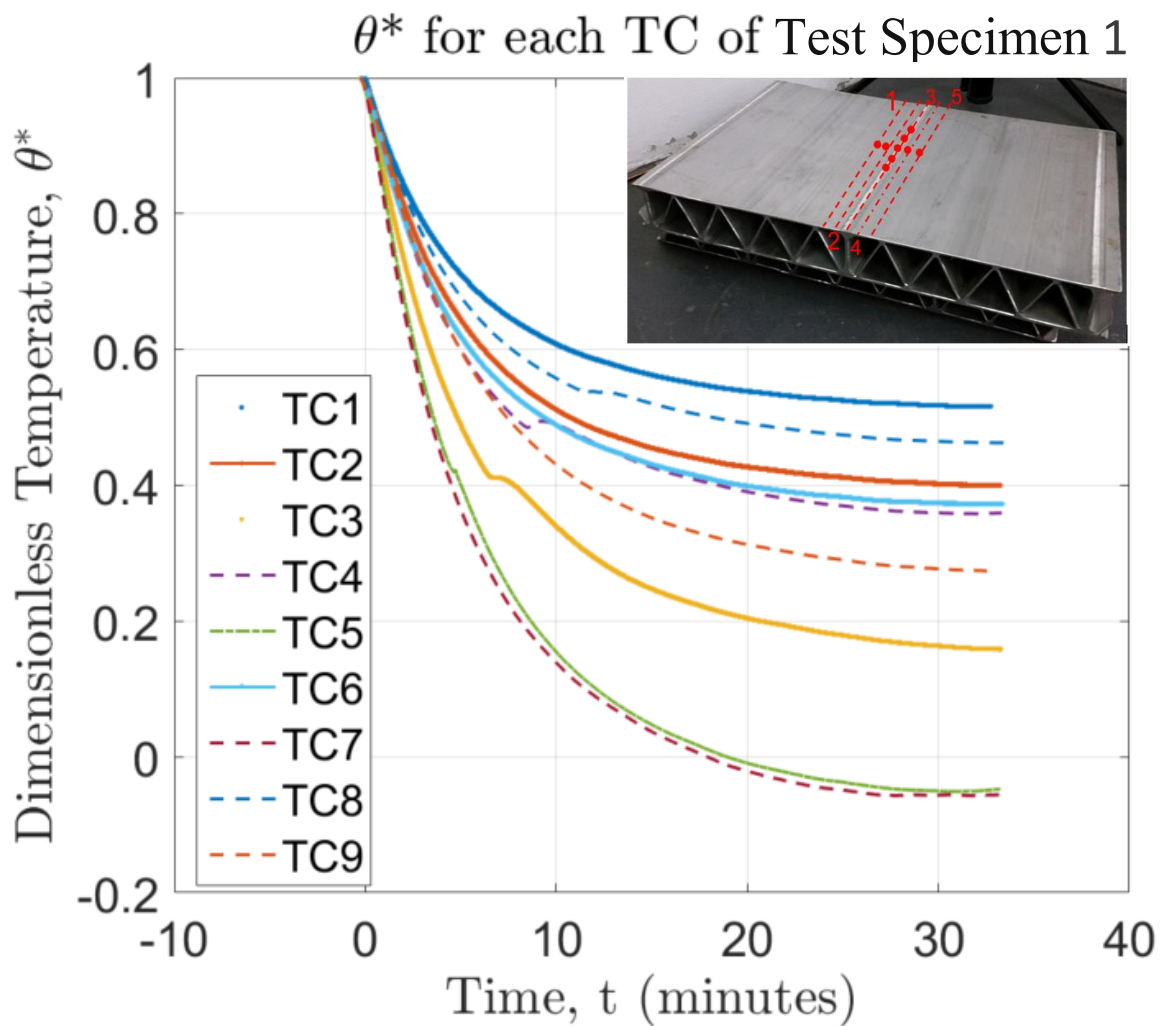


Figure 17: Phase 2 Test Specimen 1 Thermocouple Data

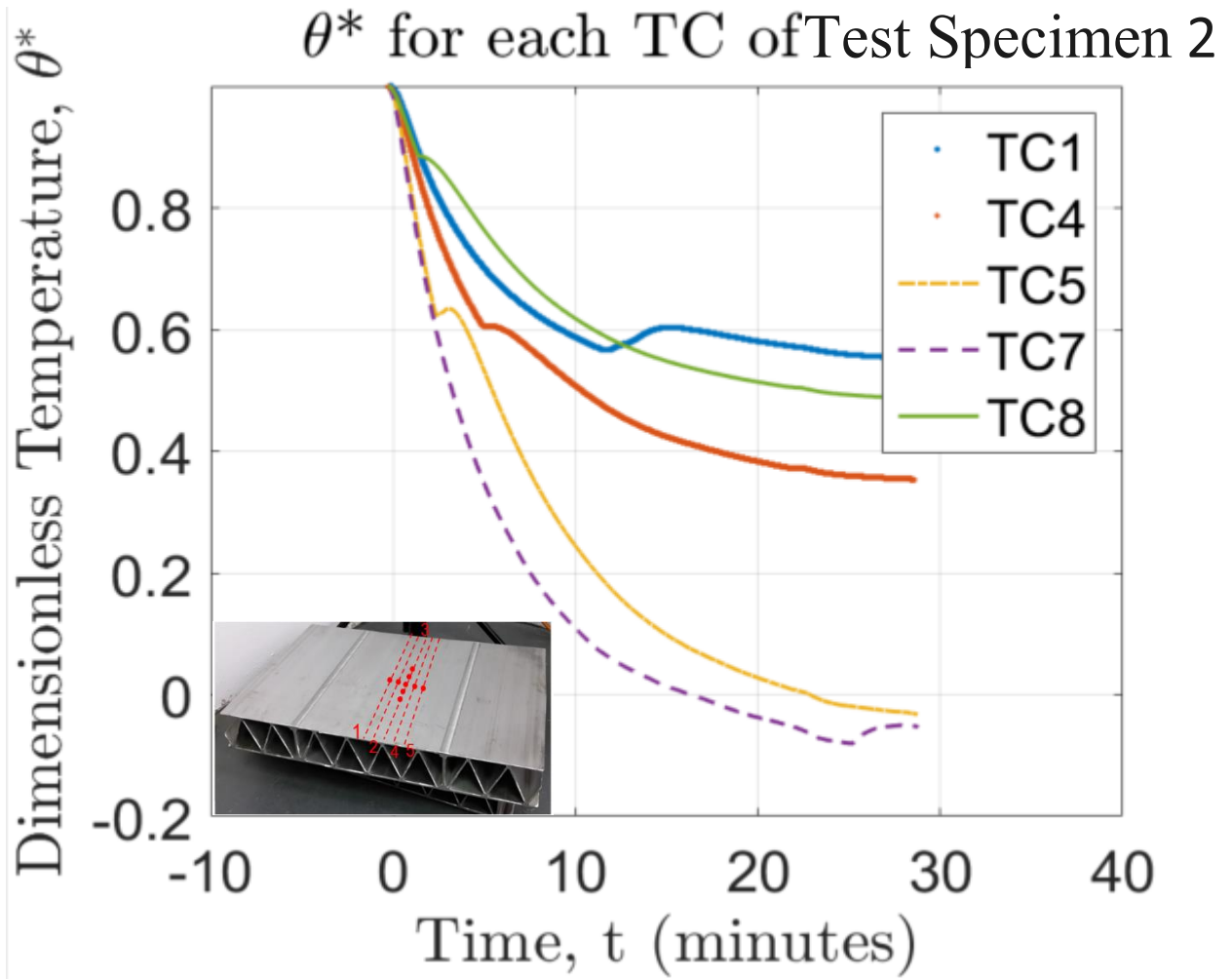


Figure 18: Phase 2 Test Specimen 2 Thermocouple Data

θ^* for TC 1 of each Test Specimen

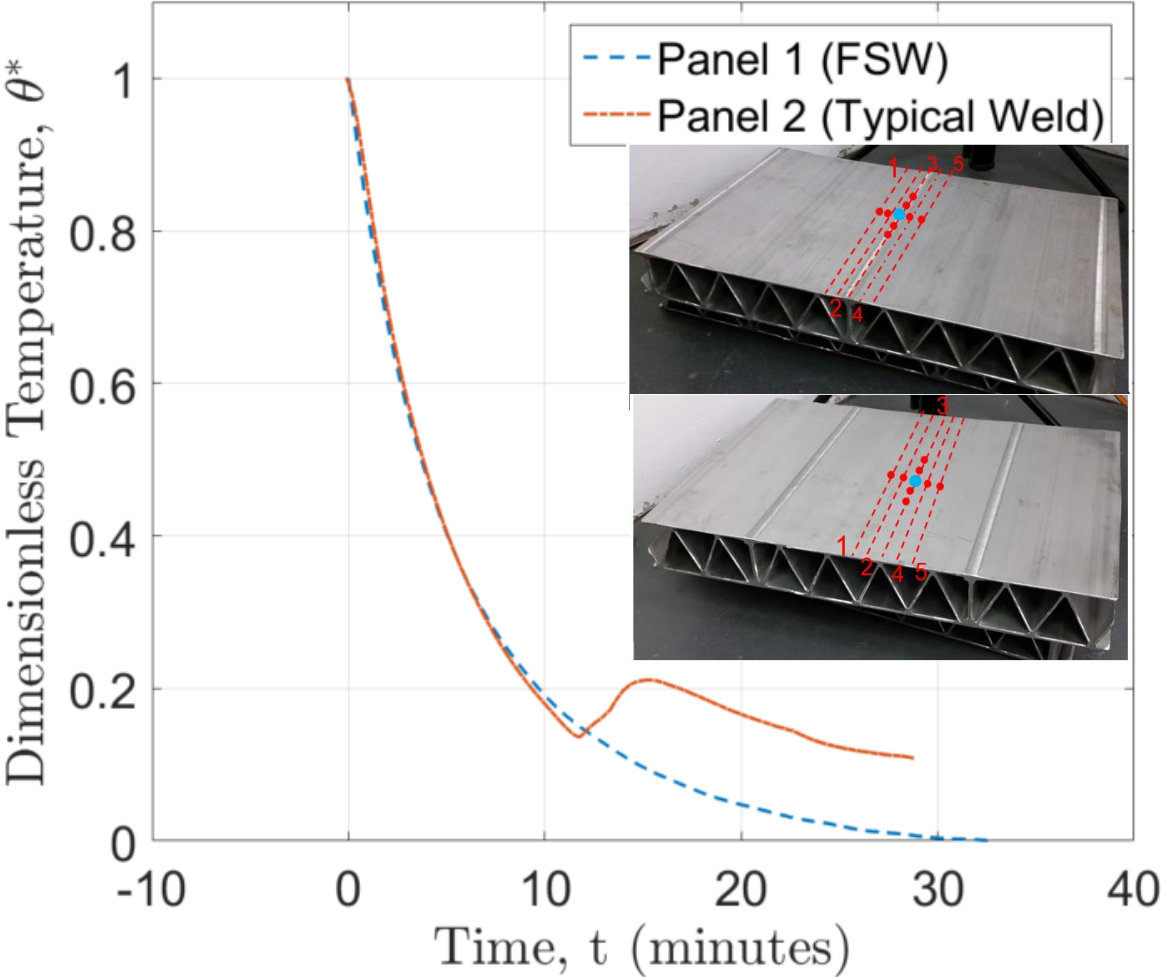


Figure 19: Phase 2 TC 1 Data for Each Test Specimen

θ^* for TC 4 of each Test Specimen

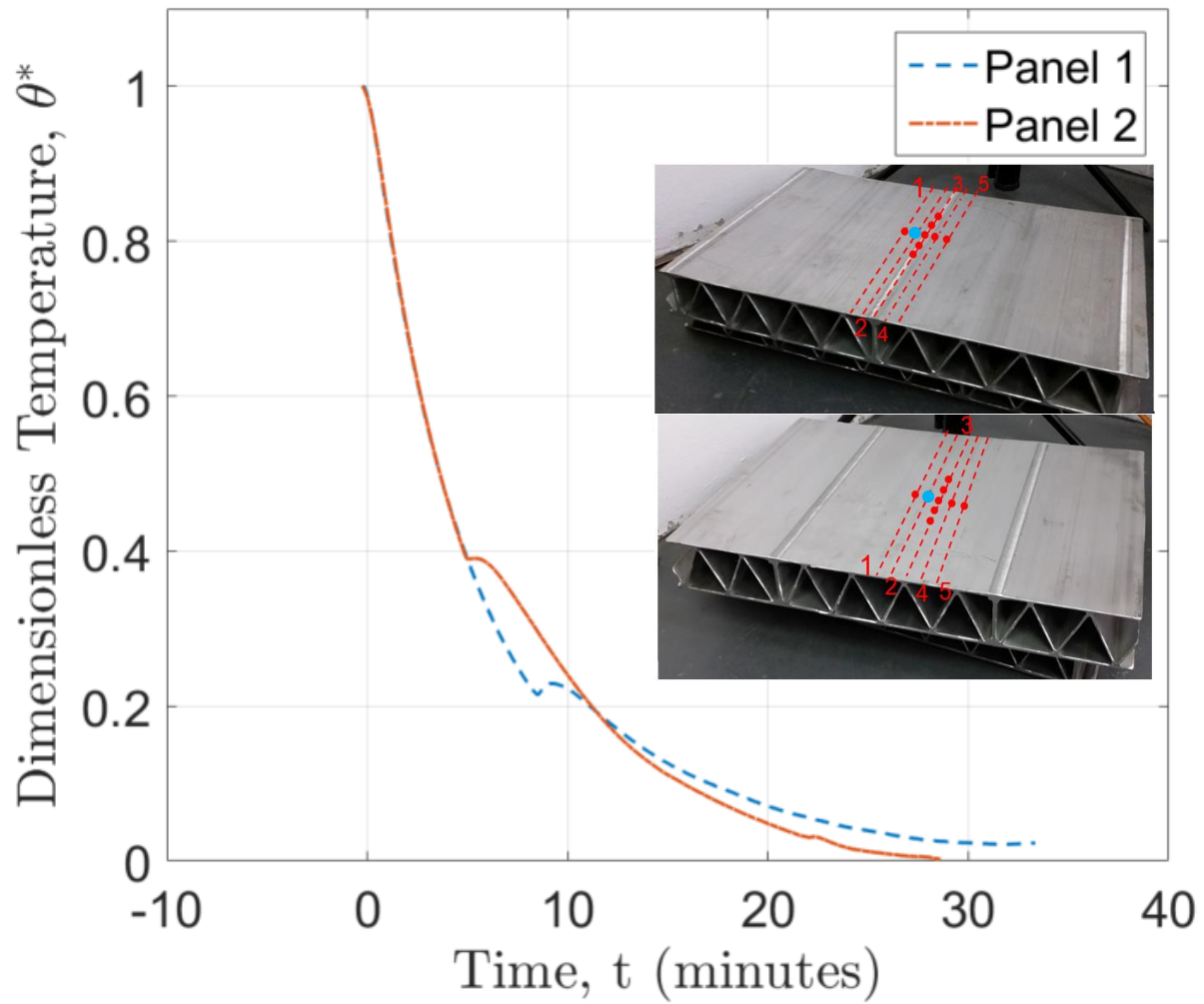


Figure 20: Phase 2 TC 4 Data for Each Test Specimen

θ^* for TC 5 of each Test Specimen

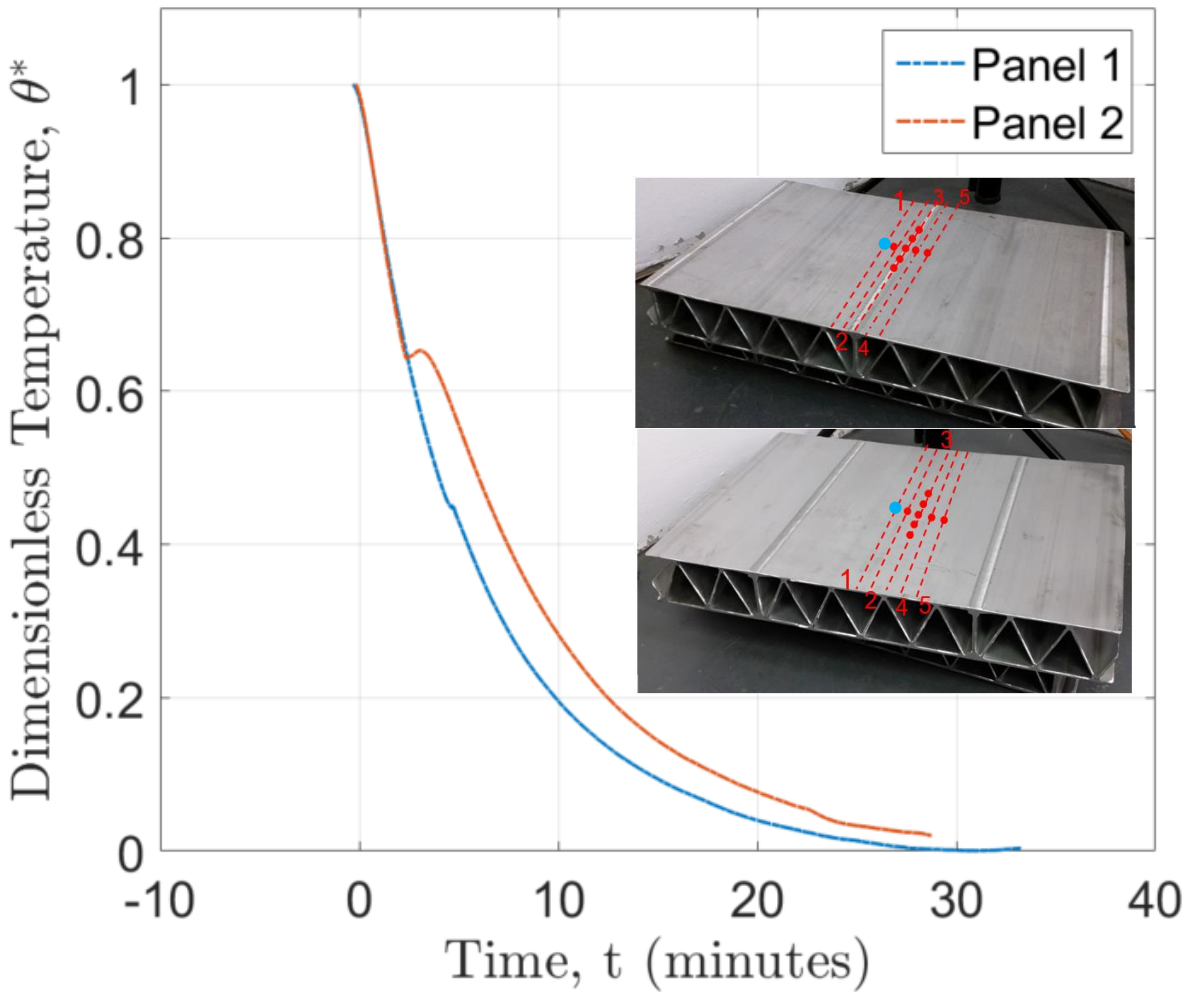


Figure 21: Phase 2 TC 5 Data for Each Test Specimen

θ^* for TC 7 of each Test Specimen

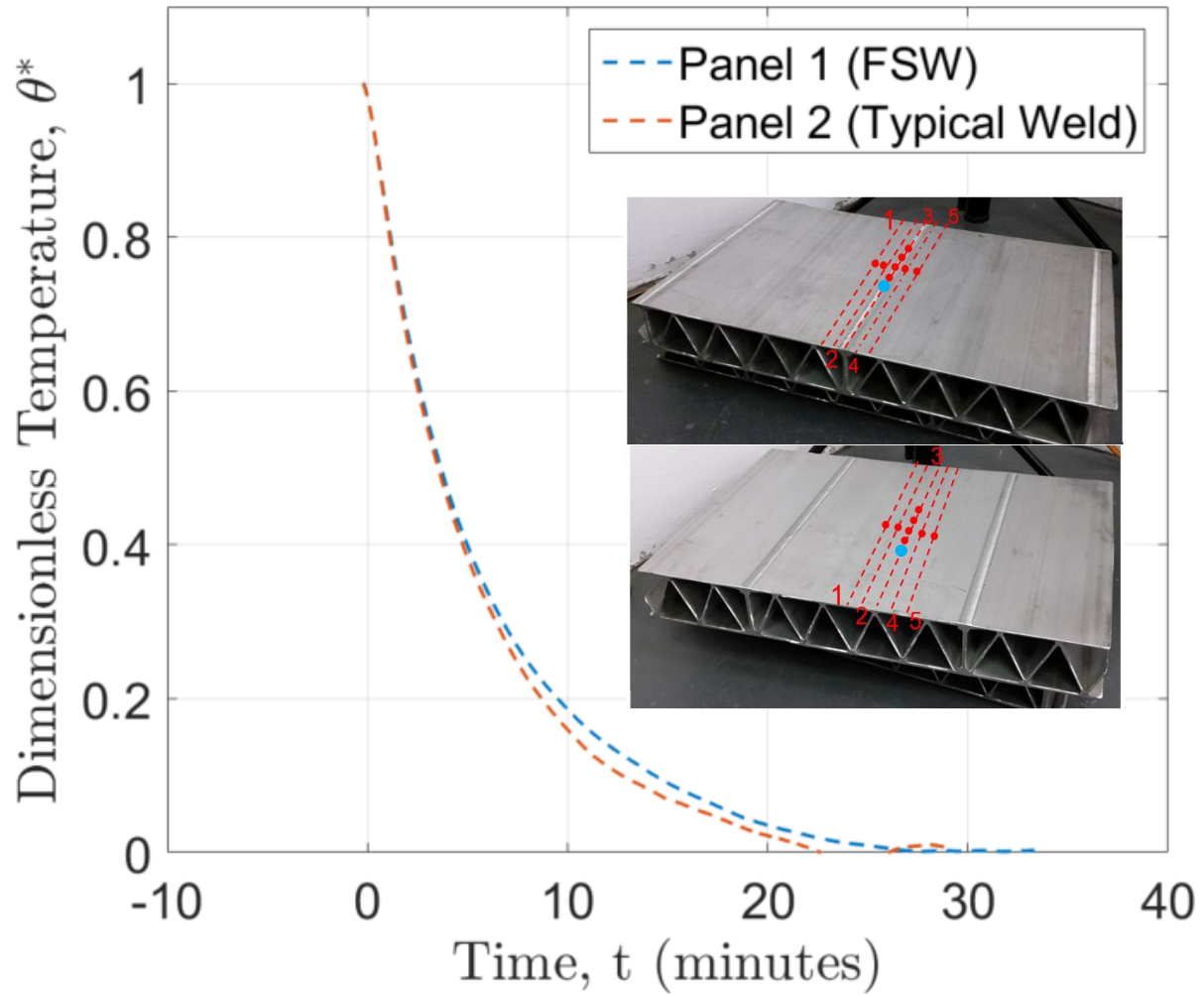


Figure 22: Phase 2 TC 7 Data for Each Test Specimen

θ^* for TC 8 of each Test Specimen

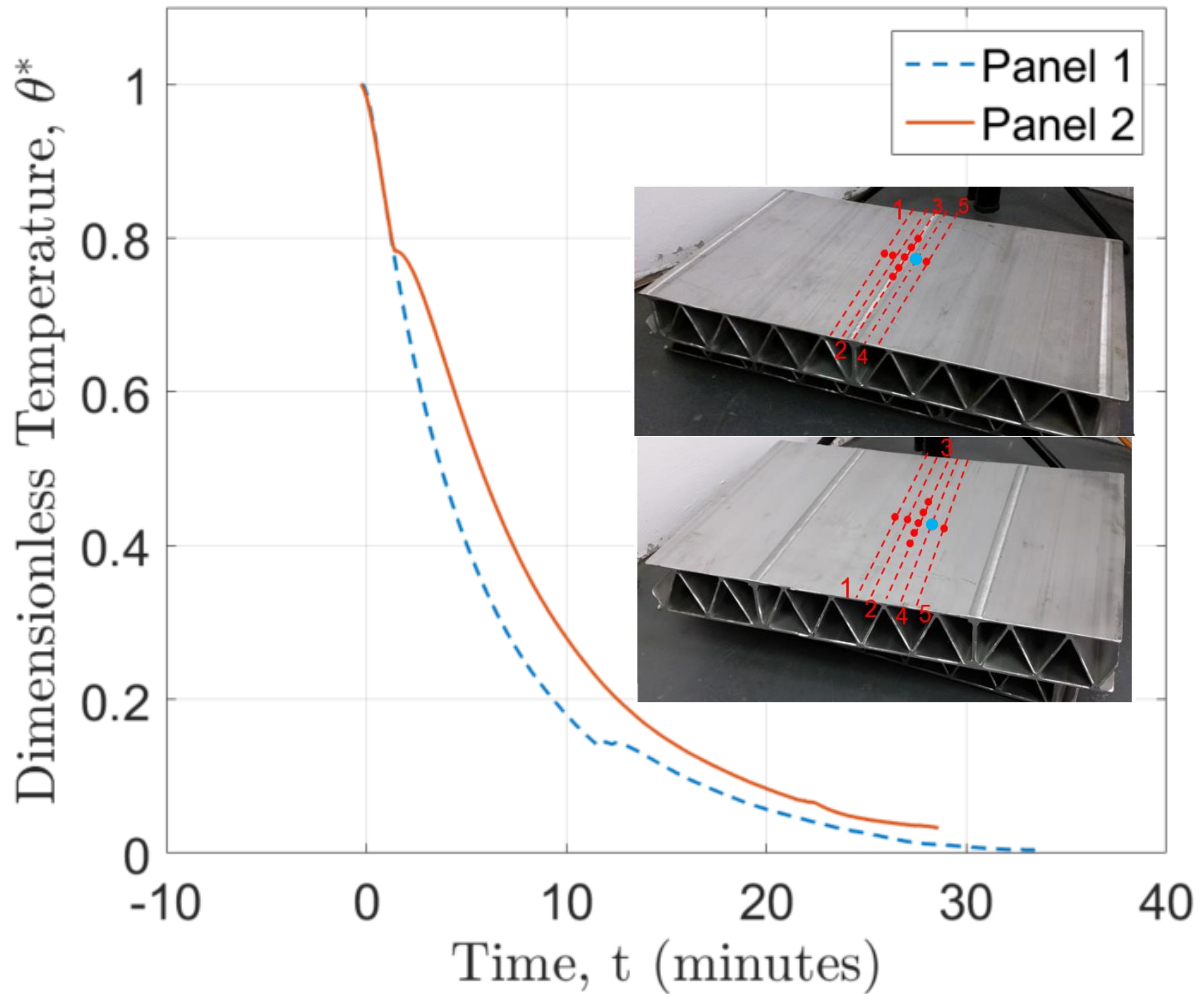


Figure 23: Phase 2 TC 7 Data for Each Test Specimen

The most interesting point to note from Figures 19-23 is the great match between the curves from the corresponding thermocouples from each specimen during the initial 10 minutes of the testing period. This is the transient portion of the test. Further, it seems that the discrepancies in the curves beyond this point are due to irregular discontinuities in several of these curves. These discontinuities indicate points at which the thermocouples became disjoined from the surface of the aluminum. This most likely occurred with the connections of more thermocouples during the aluminum testing than during the steel plate testing due to the larger thermal expansion coefficient of aluminum. Upon inspection, it was confirmed that the thermocouples which indicated discontinuities in the data had become dislodged from the surface of the specimen. However, because the insulation was wrapped to the back surface of the specimen, the thermocouples were held close to their original locations for the remainder of the tests. These minute movements of the thermocouples explain why the temperature data

at these thermocouples continues to increase in temperature along a curve consistent with a different T_{∞} value than what the curve was initially trending towards at steady state.

Despite the issues with thermocouple connectivity, it is clear that the corresponding the locations of each pair of thermocouples (i.e. TC 1 from each specimen, TC 2 from each specimen, etc.) experienced nearly the same temperatures. Considering that each specimen was exposed to the same upstream flow temperature and convection heat transfer distribution, this match of temperatures at matching locations indicates that the heat transfer modes through the specimen shows nearly no effect from the variable geometry of the corrugation between the two plates.

The center thermocouple, TC 1, on Test Specimen 1 lies directly on the FSW member. However, the center thermocouple, TC 1, on Test Specimen 2 lies directly on a typical weld. The FSW member goes straight through the thickness of the specimen, while the typical weld is connected to the front surface of the plate via a diagonal segment of corrugation (Figure 13). As such, it was expected that thermal resistance along the heat path between the center of the front surface of Test Specimen 1 through to the center of the back surface would be lower than the same resistance of Test Specimen 2. Similarly, since the corrugation from Test Specimen 1 is located with a phase shift as compared to that of Test Specimen 2 with respect to the applied thermal loads, it was expected that there would be a difference in temperature between the same points on the back surfaces of the two specimen. Furthermore, as seen in Figures 17 and 18, several of the temperature curves on an individual specimen from thermocouples at the same radial distance from the center lie nearly on top of each other. From this, it may be noted that the temperature at a given point on the back surface is dependent on the radial distance at which it is measured. Note that the thermal loads applied on the front surface of the specimen are also nearly radially symmetric. Therefore, it seems clear that the heat transfer through the specimen is more dependent on the application of thermal load than on the variation of geometry of the corrugation.

4.2.2 Infrared Images

Infrared images were taken as a means of gathering qualitative results regarding the temperature profile of each test specimen under the application of the thermal loading detailed above. Figure 24 is an infrared image of Test Specimen 1 40 minutes into the 60-minute thermal loading period. An infrared image of Test Specimen 2 at the same point in its testing cycle is shown in Figure 25. A pattern of vertical stripes interrupts the uniformity of the applied circular thermal load in each case. These stripes are indicative of the locations of the weld lines between the corrugation and the sandwich panel in each specimen. At first glance, it appears that along these weld lines temperature decreases less rapidly as radius away from the center of the specimen increases. Essentially, these weld lines seem to be pulling heat away from the center of the specimen, where the application of heat is greatest. The increase of material along these lines provides a path for heat transfer in the vertical direction (along the weld lines).

To confirm this, temperature data was extracted from Figures 24 and 25 along the lines indicated in each of the figures. The data taken from the horizontal line in each image gives a temperature profile horizontally across each specimen at this point in the thermal loading cycle. These temperature profiles are normalized by the maximum specimen surface temperature in each infrared image. It is expected that temperature dips will be visible in the horizontal temperature distributions at the radial location of each weld line. Such dips may be seen in Figures 26 & 28. As expected the dips from the welds closer to the left of the specimen surface are more extreme because these welds are nearer to the center of the jet and thus, the center of the applied thermal load.

Temperature data was also extracted from each infrared image both along the innermost weld lines and approximately halfway between these weld lines. The temperature distributions with vertical distance from the horizontal centerline for each of these lines were normalized by the maximum specimen surface temperature corresponding to each infrared image. These vertical temperature distributions are shown in Figures 27 and 29. It is apparent in both of these figures that the temperature distribution increase from the right of the panel towards the left, which is congruent with the fact that the center of the thermal load is offset slightly to the left of the center of each specimen. Additionally, it is clear that the temperatures between the weld lines are the higher than the temperatures directly along the weld lines. This further confirms that the weld lines provide a path for heat transfer and ultimately act to carry heat away from the center more so than the portions of the sandwich panel which are not in direct contact with the corrugation layer. The corrugation elements, therefore, act as heat sinks in the form of fins, pulling heat down into the thickness of the specimen.

Figure 27 depicts temperature data which was extracted along two general weld lines and also along a FSW line. Note that the overall temperature values along the FSW line are approximately the same as Weld 2. It is clear from Figure 24 that the center of the thermal load application lies directly between these two weld lines, which is why the two temperature distributions are closer together than that of Weld 1. Therefore, it appears that the type of weld does not have a clear effect on the behavior of heat transfer along the weld line. Finally, there are no visible patterns in the infrared images or dips in the temperature data along the weld lines further outward from the center in the horizontal direction despite that the weld lines occur at approximately equidistant locations throughout the entire specimen. Thus, the effect of the weld lines on the heat transfer seems to decrease greatly with the decrease in overall temperature.

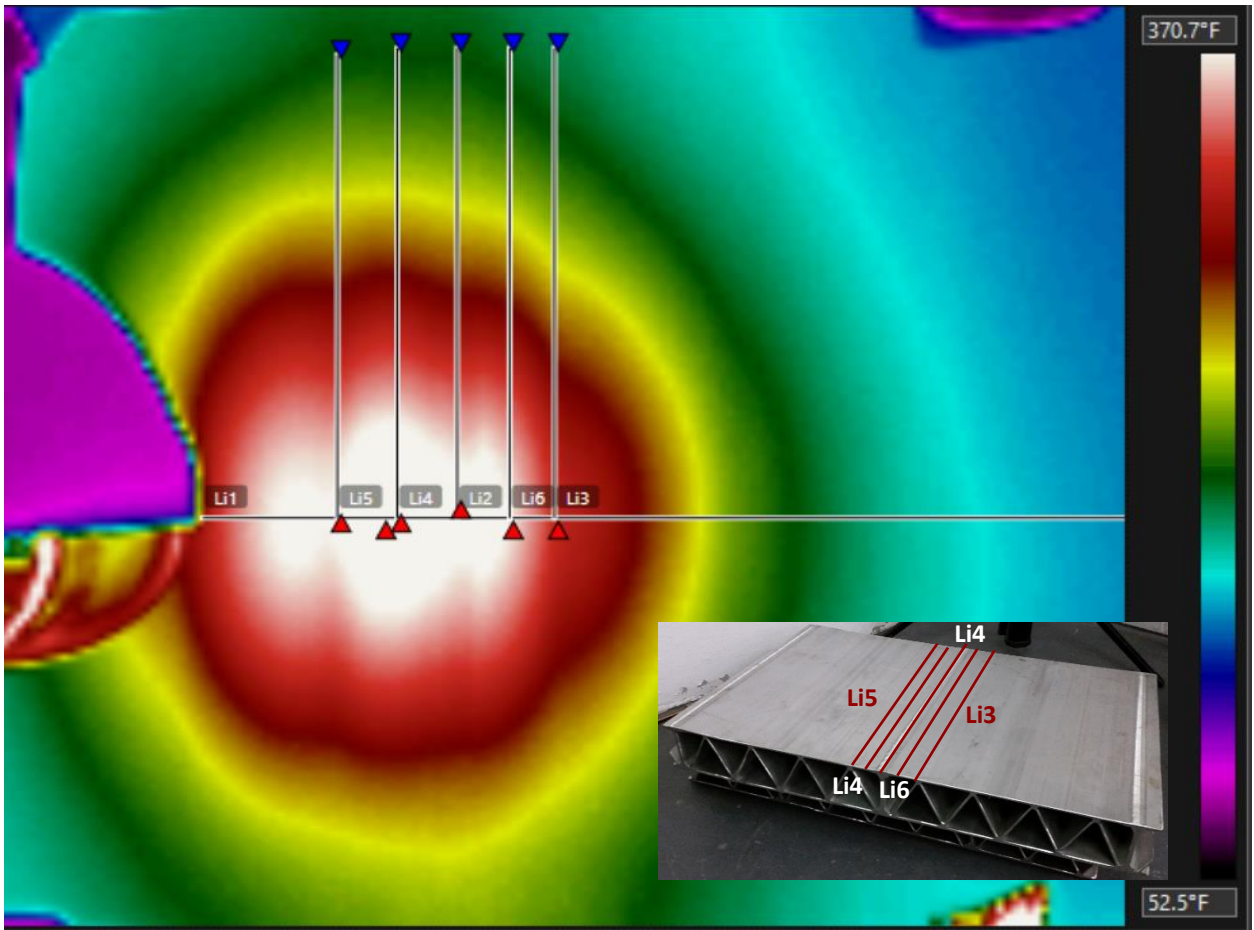


Figure 24: Phase 2 Test Specimen 1 Infrared Image, 40 Minutes into the 60-minute Loading Period

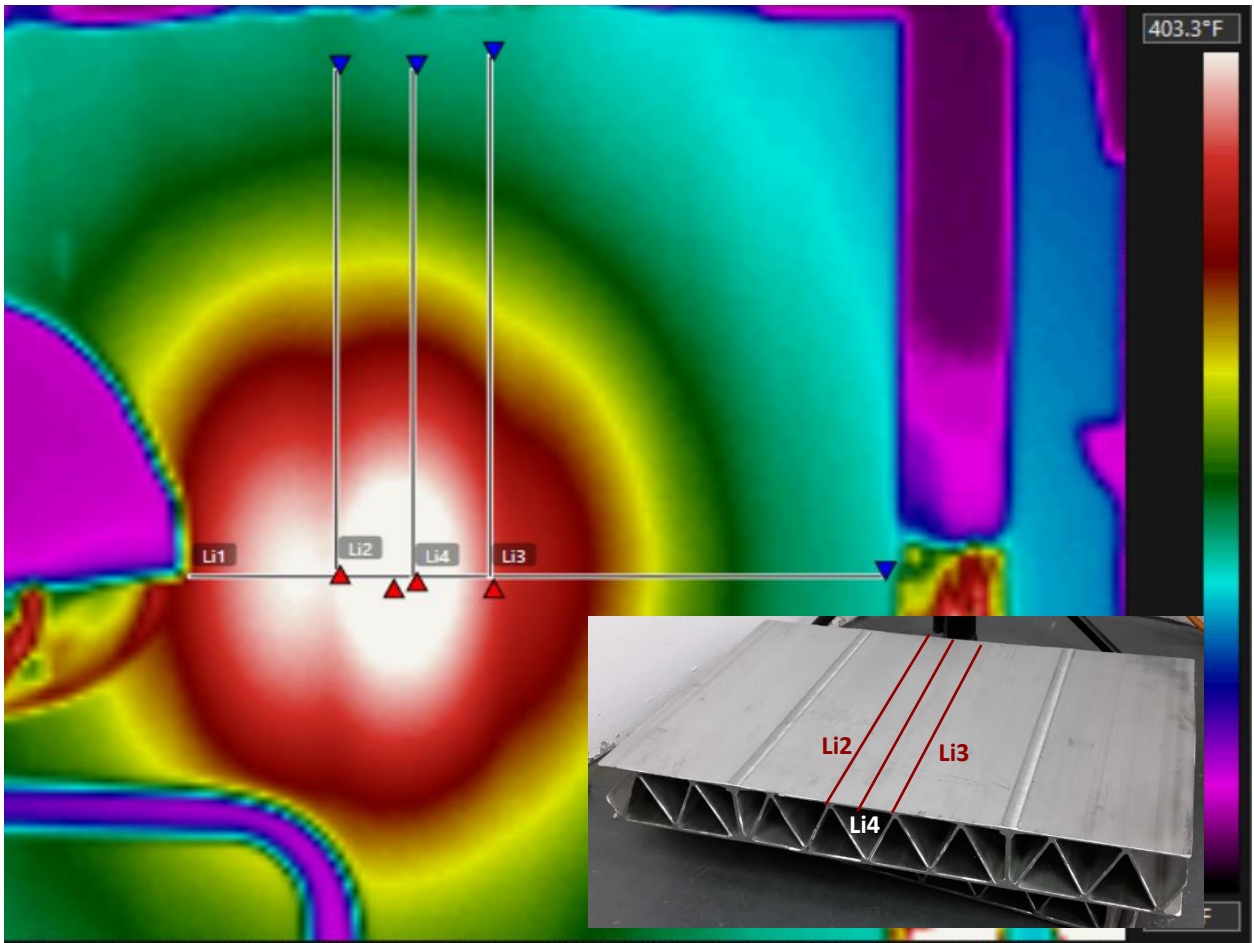


Figure 25: Phase 2 Test Specimen 2 Infrared Image, 40 Minutes into the 60-minute Loading Period

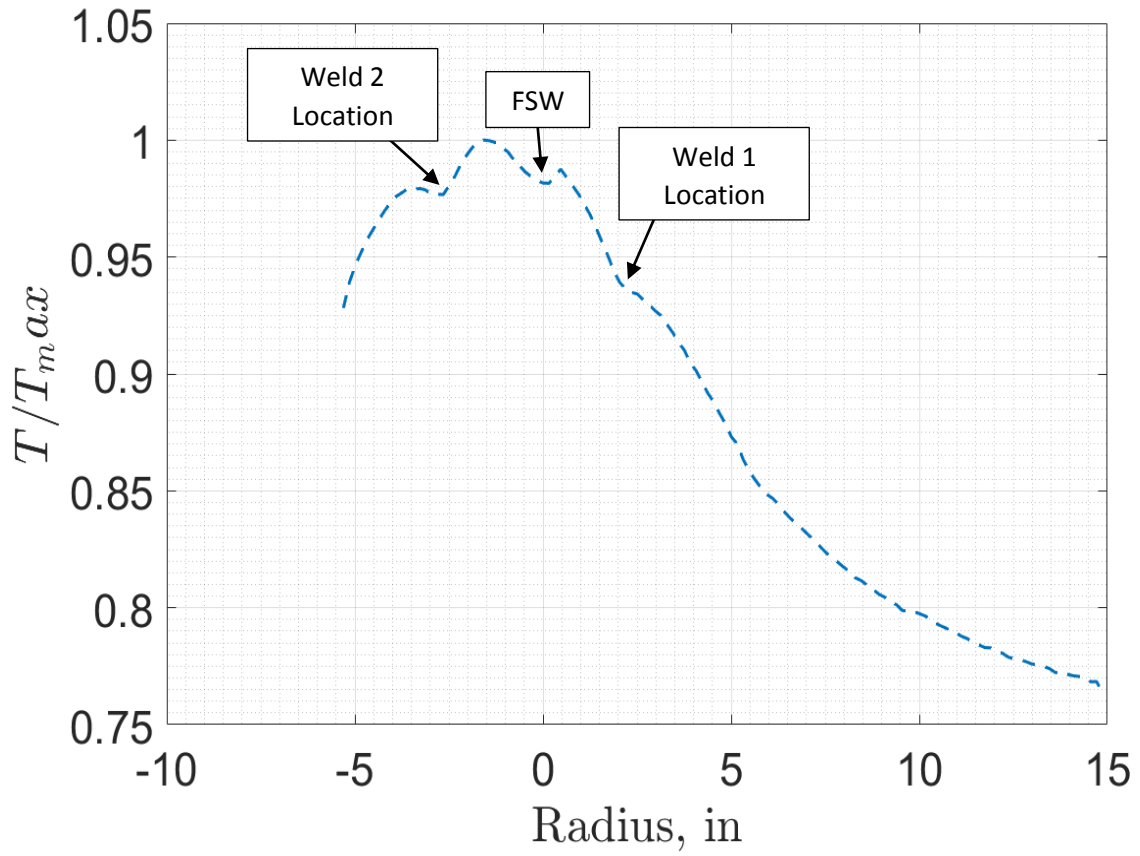


Figure 26: Phase 2 Test Specimen 1 Radial Temperature Distributions, Horizontally along the Centerline

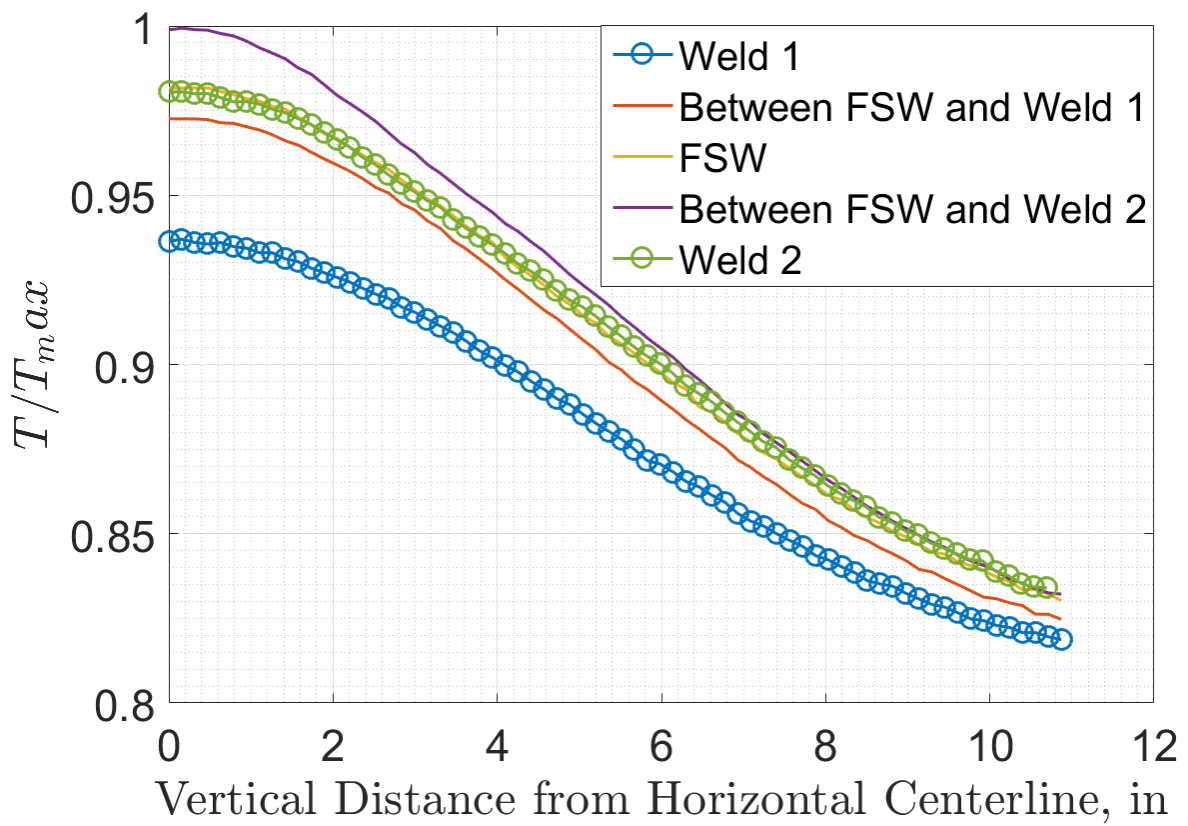


Figure 27: Phase 2 Test Specimen 1 Vertical Temperature Distributions

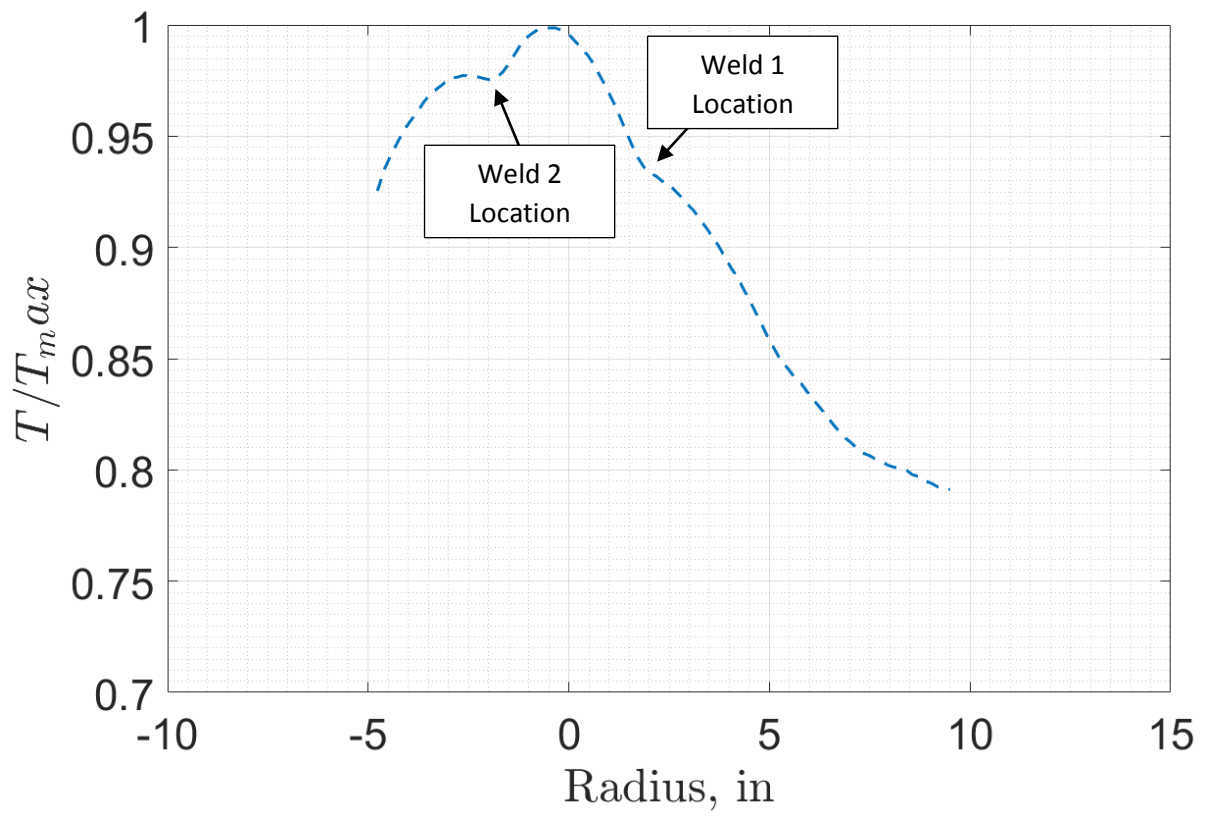


Figure 28: Phase 2 Test Specimen 2 Radial Temperature Distributions, Horizontally along the Centerline

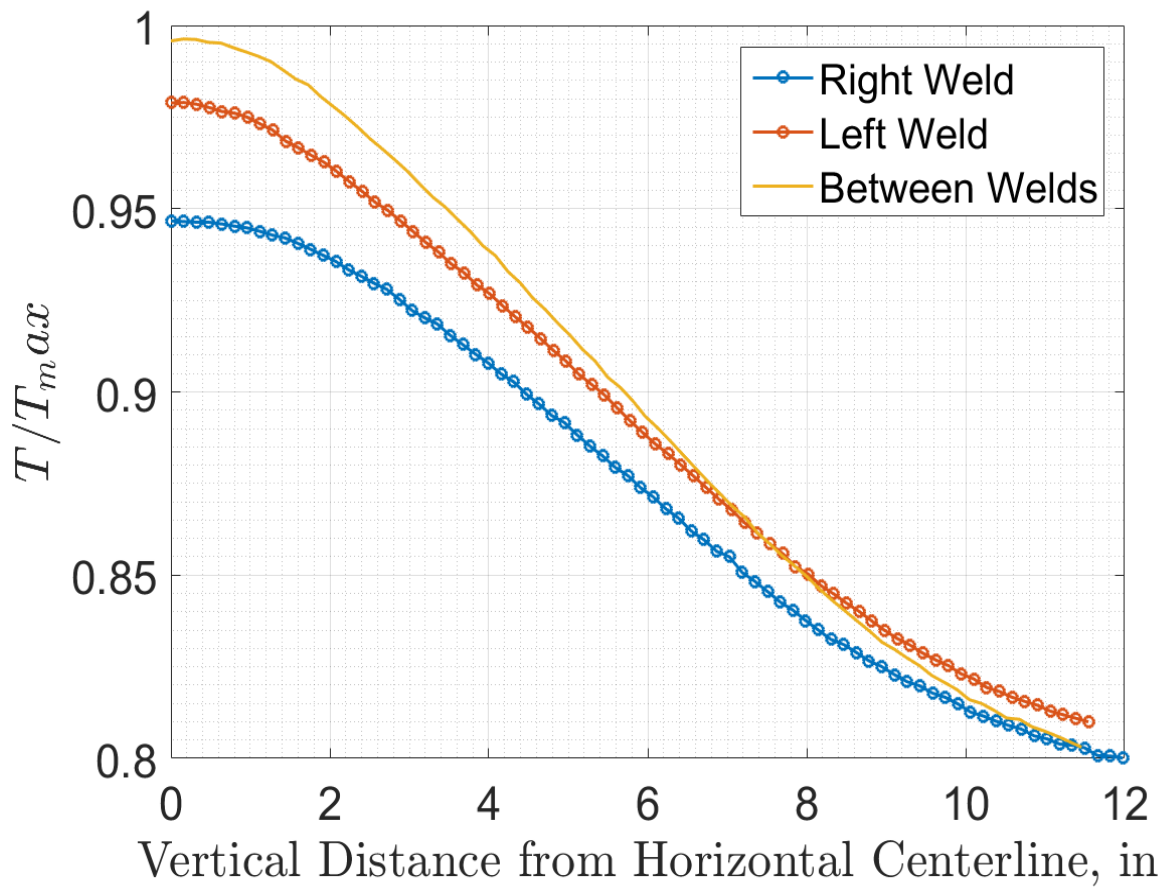


Figure 29: Phase 2 Test Specimen 2 Vertical Temperature Distributions

4.2.3 Thermal Resistance Model

Analogies to electrical circuits have commonly been used to simplify the basic concepts of many familiar systems including water flow circuits and heat flow systems [29, 30]. A thermal resistance model based on an electrical analogy was developed for the cross-section of each test specimen spanning the weld lines which showed a clear effect on heat transfer from the infrared images in the previous section. In this analogy heat is treated as electrical current and temperature acts as potential. Each segment of aluminum material in this model is treated as a resistor, since the metal segments are the available pathways for heat transfer. This model for each test specimen cross-section is depicted in Figures 30 and 31 below in which each segment is indicated as a red resistor. In these figures, each path from the top surface to the bottom surface is labeled, 1-5 for Test Specimen 1 and 1-4 for Test Specimen 2. Resistance from all of these paths was then used to determine the total resistance from any given point on the upper surface of the specimen to any given point on the lower surface of the specimen. The resistances along each path were solved using Equation 15 below [31].

$$\frac{R_{path}}{L} = \int_{s_0}^{s_1} \frac{ds}{k_{alum} t} \quad (15)$$

Each resistance per unit length corresponding to each path was then summed to get the total resistance from any point on the top surface to any point on the bottom surface of the specimen. This is calculated using Equation 16, in which there are i paths.

$$\frac{1}{R_{total}} = \sum_1^i \frac{1}{R_i} \quad (16)$$

Figures 32 and 33 summarize the findings of these calculations by mapping out the total resistance from any point on the upper surface to any point on the lower surface by summing the resistances along each path labeled in Figures 30 and 31. This assumes heat travels only along these paths and that heat transfer through air in the corrugation is comparably negligible. The ordinate axis in Figures 32 and 33 show all points on the upper surface of the specimen and the abscissa indicates all points on the lower surface. Both axes values are normalized by cross-sectional height. Therefore, in order to determine the resistance between any given points on the upper and lower surface, one must first find where that upper surface point corresponds to on the ordinate axis and then slide over to find where that intersects with the point of interest on the lower surface. Figure 32 agrees with the expectation that the path of least resistance through Test Specimen 1 is directly from the upper surface to the lower surface via the FSW member at the center of the cross-section (path 3). Additionally, Figure 33 confirms the expectation that the path of least resistance from the upper surface to the lower surfaces are either paths 2 or 3, equally. Finally, as one would expect, the greatest resistance path runs from either corner on the upper surface to the opposite corner on the

bottom surface. In Figure 33 for example, this could be read from approximately -1 on the upper surface to 1 on the lower surface. Clearly, in figure 33, that point is one of greatest resistance.

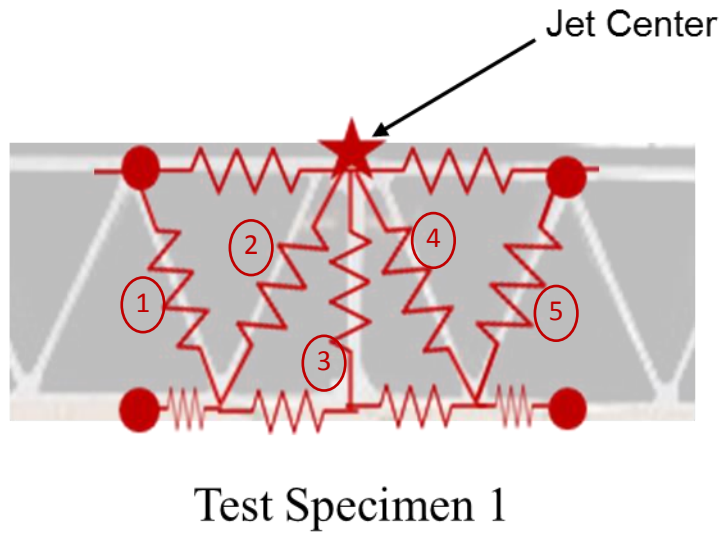


Figure 30: Test Specimen 1 Cross-section Thermal Resistance Model

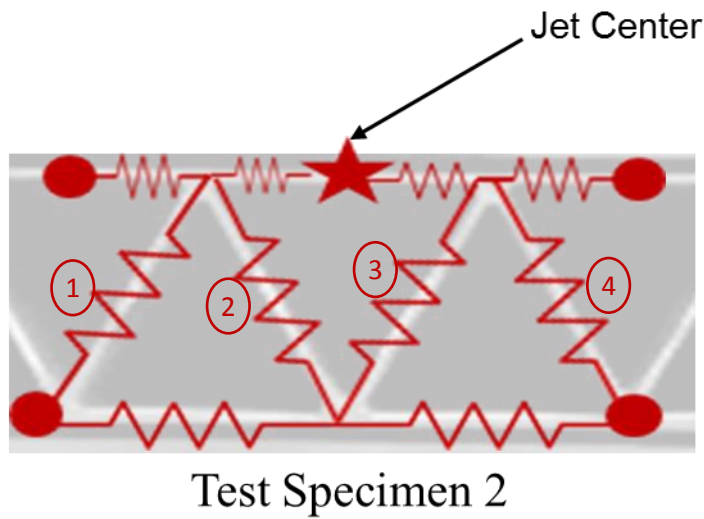


Figure 31: Test Specimen 1 Cross-section Thermal Resistance Model

Thermal Resistance Across Test Specimen 1 Cross-section

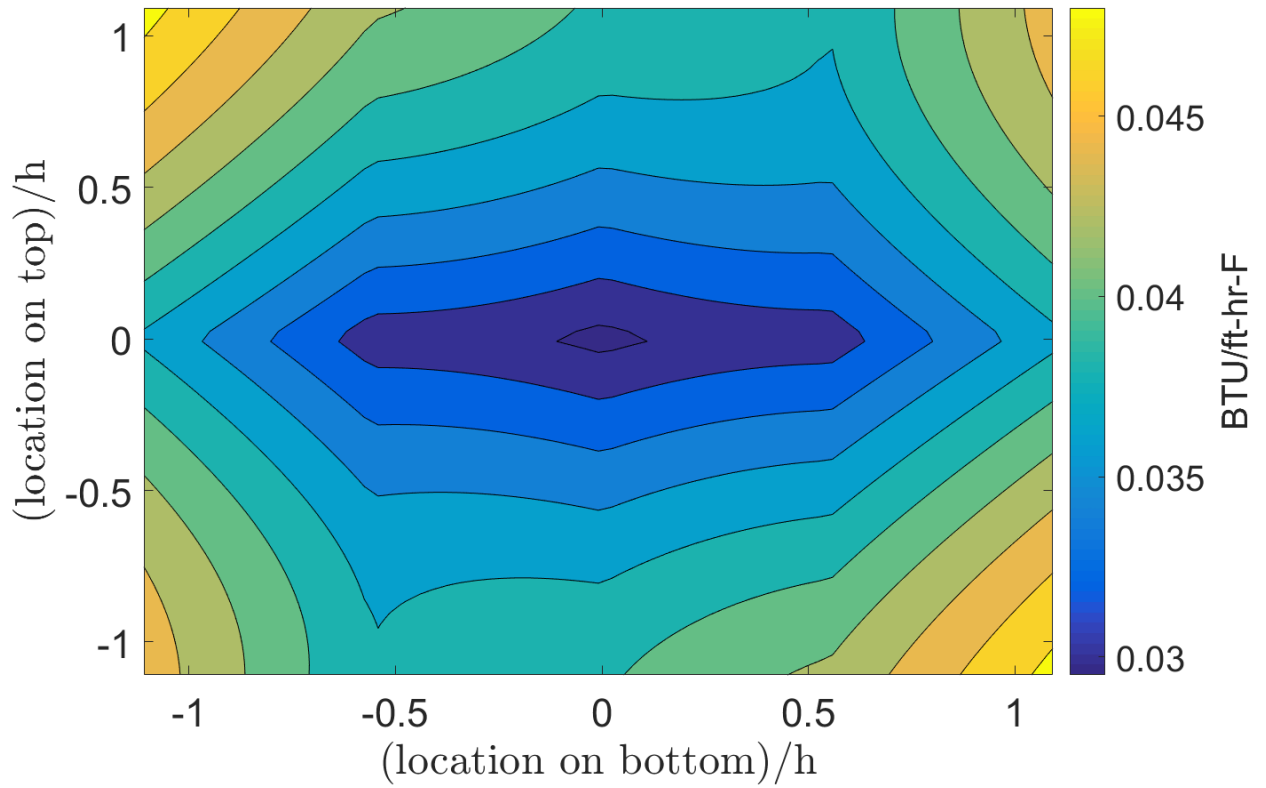


Figure 32: Test Specimen 1 Cross-section Thermal Resistance Map from Upper to Lower Surface

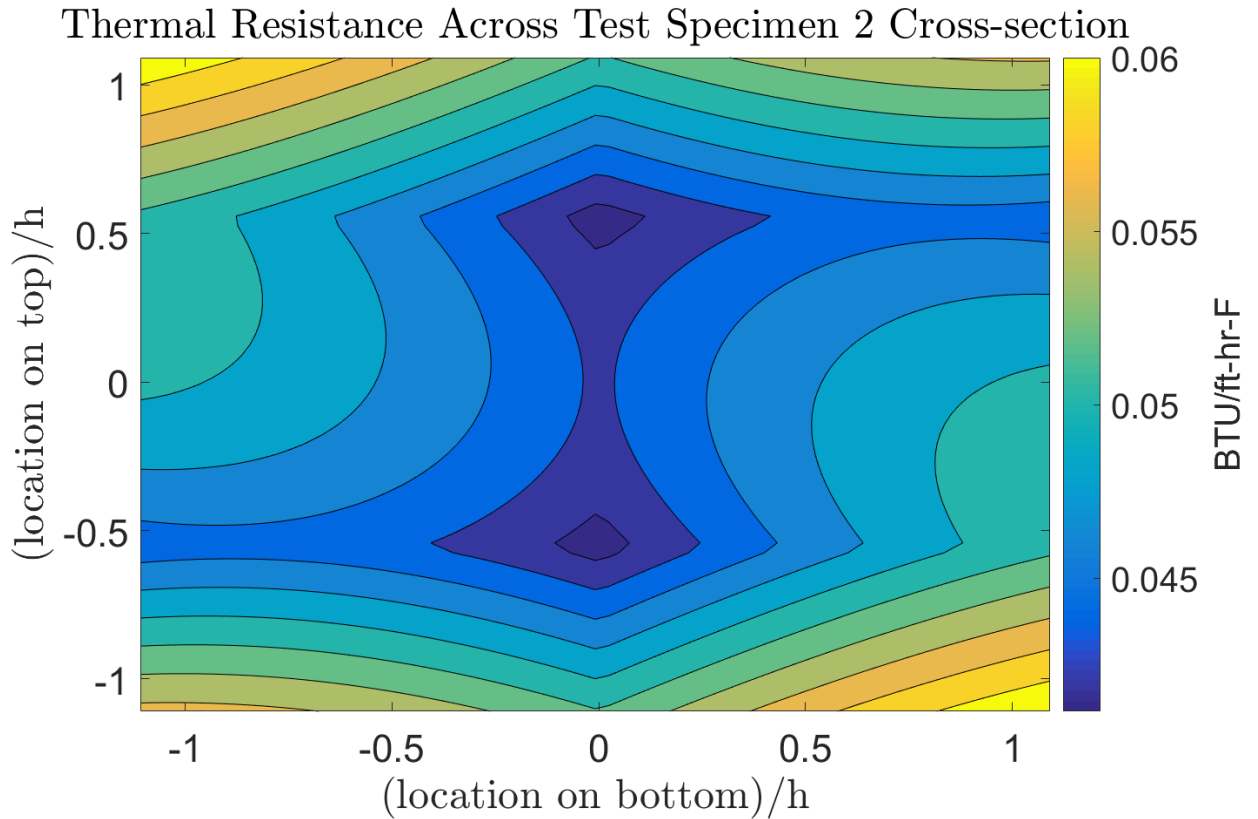


Figure 33: Test Specimen 2 Cross-section Thermal Resistance Map from Upper to Lower Surface

By compiling the qualitative images from both the thermocouple data and the infrared images and determining the paths of least and greatest resistance from the thermal resistance model, a qualitative phenomenological schematic of heat transfer through each test specimen may be developed. The infrared images indicates dips in temperature along the weld lines attached to the front surface of each specimen; Figures 17 and 18 also indicate a decay in temperature with radius outward from the center of the back surface of each specimen. Finally, Figures 34 and 35 indicate the logical flow of heat evidenced by both categories of data. Note that in these images, darker and thicker heat flow arrows indicate larger heat flux along those paths.

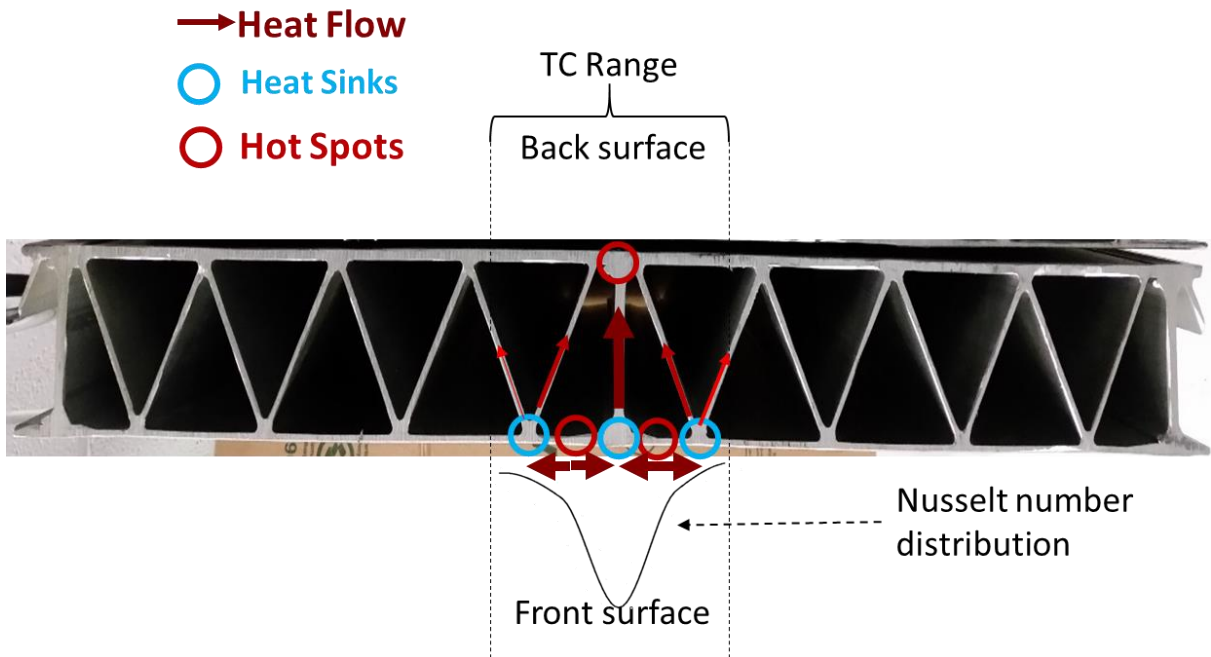


Figure 34: Qualitative Phenomenological Heat Transfer Schematic for Test Specimen 1

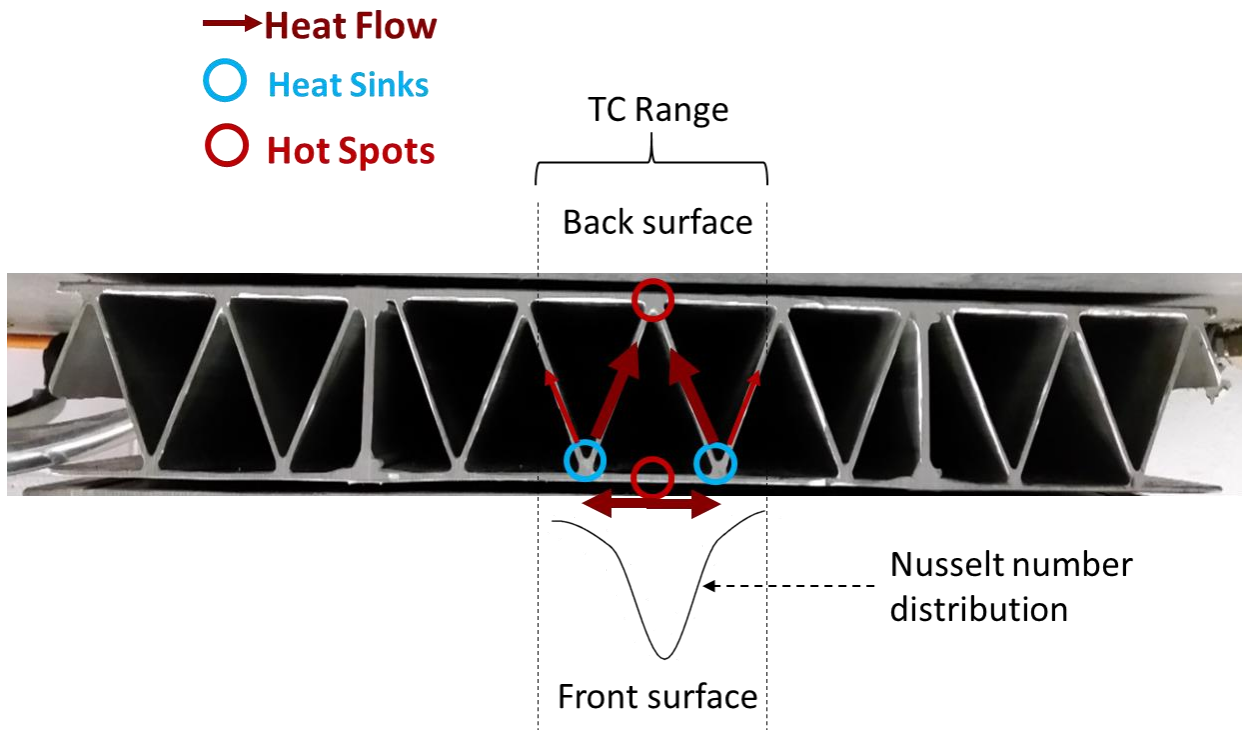


Figure 35: Qualitative Phenomenological Heat Transfer Schematic for Test Specimen 2

4.3 Uncertainty Study for Nusselt Number

In order to gain an understanding of the effects of perturbations of each variable on the final results for Nusselt number, a simple uncertainty study was conducted for the case of the center thermocouple on Test Specimen 1. First, the variables upon which the Nusselt number is dependent must be identified. Based on Equations 6, it may be noted that the local effective thickness, $Nu = Nu(\mathbf{h}, \mathbf{D}_j)$. Furthermore, as outlined in §3.6.1 and §4.1, the convection heat transfer coefficient value is found by fitting a theoretical L.C.M model curve to thermocouple data from Phase 1 tests. Therefore, from the L.C.M model, given in Equation 6, h itself will be dependent on several variables. Specifically, $\mathbf{h} = \mathbf{h}(T, T_\infty, T_i, \mathbf{b}_s)$, where \mathbf{b}_s is the true thickness of the steel plate used for testing in Phase 1. However, any perturbations in the values of T will simply shift the full temperature curve, not changing the shape of the curve. The values of \mathbf{h} and \mathbf{b}_s are dependent on the shape of the curve, and are thus not altered by a shift. Similarly, perturbations in the value of T_i merely extend or shorten the initial linear portion of the temperature curve. This also does not change the shape of the curve, and consequently has no effect on the values of \mathbf{h} or \mathbf{b}_s . Therefore, the local effective thickness becomes dependent on only two variables, $Nu = Nu(\mathbf{b}_s, T_\infty, \mathbf{D}_j)$.

Common uncertainty models evaluate the effect of a perturbation of each individual variable on the overall result. Such a model is given below in Equation 17 [32].

$$\delta F(x, y, z) = \sqrt{\left(\frac{\delta F(x, y, z)}{\delta x} \delta x\right)^2 + \left(\frac{\delta F(x, y, z)}{\delta y} \delta y\right)^2 + \left(\frac{\delta F(x, y, z)}{\delta z} \delta z\right)^2} \quad (17)$$

In the case of the local effective thickness at TC 1 on Test Specimen 1, this becomes,

$$\delta Nu = \sqrt{\left(\frac{\delta Nu}{\delta b_s} \delta b_s\right)^2 + \left(\frac{\delta Nu}{\delta T_\infty} \delta T_\infty\right)^2 + \left(\frac{\delta Nu}{\delta D_j} \delta D_j\right)^2} \quad (18)$$

The measured values for each variable and the Nusselt number for this case are shown in the Table 6 below. The effect of uncertainties in each variable was then assessed by calculating the change in effective thickness, assuming no perturbation in the variable not being evaluated while perturbing the other variable over a range from 0-100%.

Table 6: Unperturbed Variable Values

| Variable | Unperturbed Value |
|------------|-------------------|
| Nu | 203 |
| b_s | 0.2083' |
| T_∞ | 515°F |

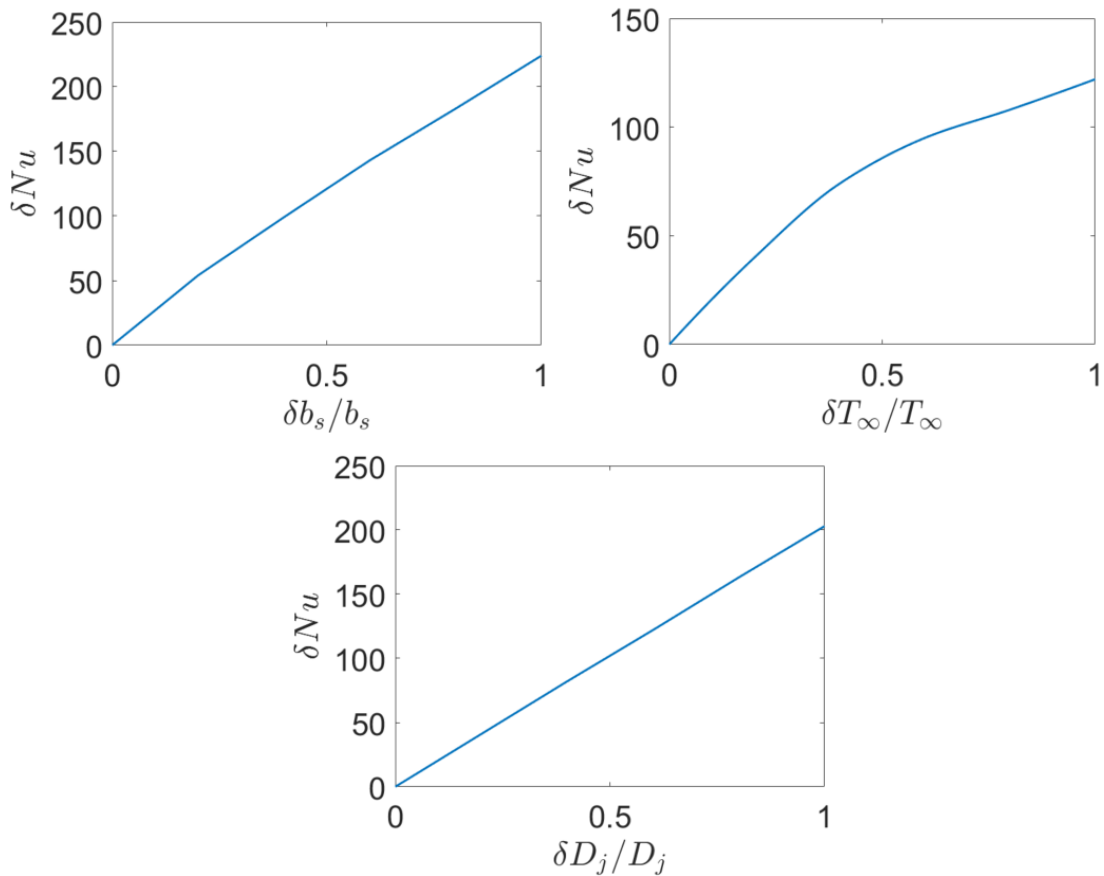


Figure 36: Uncertainty in Nusselt Number at TC 1 on Test Specimen 1 due to Perturbation of Steel Plate Thickness, Fluid Temperature Upstream of the Specimen, and Jet Diameter

From Figure 36, it may be seen that the percent perturbation of steel plate thickness and the jet diameter have a nearly linear effect on the Nusselt number on the front surface of the steel plate. Additionally, the effect of perturbation is less than 50% below a 50% perturbation for all variables. However, the percent perturbation of T_∞ is not linear. Rather it has a trend qualitatively closer to exponential.

5. Conclusions

Overall, this work sought to assess the heat transfer effects of application of the thermal loads similar in nature to those generated by exhaust plume of a VTOL aircraft on aluminum alloy ship deck panels. In the first phase of testing, a thermal loading distribution was characterized by convection heat transfer coefficient and total temperature values. During this phase, the appropriate facility settings and test set-up to repeat this loading were determined. In Phase 2 of testing, two types of temperature data were collected to gain an understanding of both the transverse heat transfer across the surface of the specimen to which heat was applied and the heat transfer through the thickness of the specimen. Firstly, thermal images were collected using a FLIR A655sc thermal imaging camera. These images were assessed qualitatively to locate the primary heat paths on the surface of the specimen. Thermocouple data was also collected on the back surface of the specimen and was used to ultimately determine the most likely heat paths through each specimen along with the effects of the variable geometry of the corrugation between the two specimen. Ultimately, the primary findings of this study were:

- 1) The weld lines adjacent to the front surface plate on each specimen act to wick heat away from the point of application, generating dips in the radial front surface temperature profile which correspond to the location of the weld lines.
- 2) The heat transfer through the corrugated deck panels is dominantly dependent upon the application of thermal loads and shows no clear dependence on the variation of corrugation geometry.

Finally, it would be the recommendation of the author based upon this study to alleviate the unwanted heat transfer through the full thickness of the corrugated deck panels by introducing air flow (or an alternative coolant) through the corrugation channels. This solution would take advantage of the inherent heat sink nature of the corrugation, essentially treating them as fins exposed to convection heat transfer through the panels. Designs very similar to this corrugated sandwich panel-surface plate configuration are often even used as heat exchangers for their ability to enhance heat transfer away from the heated surface and out of the exchanger element [33 -35].

References

- [1] Sielski, R.A. “The History of Aluminum as a Deckhouse Material”, *Naval Engineering Journal* 99, 165-172, 1987.
- [2] Sielski, R.A. *Research Needs in Aluminum Structure*. American Bureau of Shipping, 10th International Symposium on Practical Design of Ships and Other Floating Structures, Houston, TX, 2007.
- [3] Zubaly, R. B., *Applied Naval Architecture*. Schiffer Publishing Ltd., Atglen, PA 2011.
- [4] Associated Press, “Navy Reverting to Steel in Shipbuilding after Cracks in Aluminum,” *The New York Times*, Aug. 1987.
- [5] Reutzler, E.W., and Koudela, K.L. “Lightweight Laser-Welded Stiffened Structures”. *iMast Quarterly*, No. 1, pp 3-6. 2001.
- [6] Gauntner, J.W., Livingood, J.N.B., and Hrycak, P., “Survey of Literature on Flow Characteristics of a Single Turbulent Jet Impinging on a Flat Plate”, NASA TN D-5652, 1970.
- [7] Incropera, F.P., Dewitt, D.P., Bergman, T.L, and Lavine, A.S., *Fundamentals of Heat and Mass Transfer*, 6th ed., John Wiley & Sons, Hoboken, NJ 2007.
- [8] Schetz, J.A., and Bowersox, R. D.W., *Boundary Layer Analysis*, 2nd ed., AIAA Education Series, AIAA, Reston, VA 2011.
- [9] Hornung, H.G., *Dimensional Analysis: Examples of the use of Symmetry*. Dover Publications, Mineola, NY 2006.
- [10] Englerth, S.T., “An Experimental Conduction Error Calibration Procedure for Cooled Total Temperature Probes” , MS Thesis, Aerospace and Ocean Engineering Department, Virginia Polytechnic Institute & State University, Blacksburg, VA, Feb. 2015.
- [11] Andron, P., “Nominal Thermal Input Criteria for Flight Deck Design”, NSWCCD, West Bethesda, MD 2014.
- [12] Kerlin, T.W., and Johnson, M., *Practical Thermocouple Thermometry*, International Society of Automation, Research Triangle Park, NC 2012.
- [13] Reardon, J.P., “Computational Modeling of Radiation Effects on Total Temperature Probes”, MS Thesis, Aerospace and Ocean Engineering Department, Virginia Polytechnic Institute & State University, Blacksburg, VA, Dec. 2015.
- [14] Mikic, B.B, and Rohsenow, W.M., “Thermal Contact Resistance”, M.I.T. TR 4542-41, Massachusetts Institute of Technology Department of Mechanical Engineering, Cambridge, MA 1966.

- [15] Martin, W. R., and Weir, J. R., "Mechanical Properties of X8001 and 6061 Aluminum Alloys and Aluminum-Base Fuel Dispersion at Elevated Temperatures", Rep. no. ORNL-3557, Oak Ridge National Laboratories, Oak Ridge, TN, 1964.
- [16] ASM International, Handbook Committee. *Properties and Selection: Nonferrous Alloys and Special- Purpose Materials*, Vol. 2, 10th ed., ASM International, US 1990.
- [17] Summers, P.T., Yanyun, C., Rippe, C.M., Allen, B., Mouritz, A.P., Case, S.W., Lattimer, B.Y., "Overview of aluminum alloy mechanical properties during and after fires," *Fire Science Reviews*, Springer, 2015.
- [18] Ekkad, S.V. "Virginia Tech Advanced Propulsion and Power Lab (VT APPL)", National Energy Technology Laboratory, 2015.
- [19] Brooks, D.R., "Development of Specialized Laser Doppler Velocimeters for High Resolution Flow Profile and Turbulence Spectral Measurements" , MS Thesis, Aerospace and Ocean Engineering Department, Virginia Polytechnic Institute & State University, Blacksburg, VA, April 2014.
- [20] Witze, P.O., "Centerline Velocity Decay of Compressible Free Jets", Sandia Laboratories, Livermore, CA, April 1974.
- [21] Maranzana, G., Didierjean, S., Rémy, B. and Maillet, D., "Experimental estimation of the transient free convection heat transfer coefficient on a vertical flat plate in air," *International Journal of Heat and Mass Transfer* 45, 3413-3427, 2002.
- [22] Sarkar, A. and Singh, R.P., "Spatial Variation of Convective Heat Transfer Coefficient in Air Impingement Applications," *Journal of Heat Transfer* 68, 910-916, 2003
- [23] Wang, C.C., Chung, B.T.F., and Thomas, L.C., "Transient Convective Heat Transfer for Laminar Boundary Layer Flow with Effects of Wall Capacitance and Resistance," *Journal of Heat Transfer* 99, 513-519, 1977.
- [24] Metzger, D.E. and Grochowsky, L.D., "Heat Transfer Between an Impinging Jet and a Rotating Disk," *Journal of Heat Transfer* 99, 663-667, 1977.
- [25] Chen, Z., Gu, M., and Peng, D., "Heat transfer performance analysis of a solar flat-plate collector with an integrated metal foam porous structure filled with paraffin," *Applied Thermal Engineering* 30 1967-1973, 2010.
- [26] Popiel, C.O., and Wojtkowiak, J., "Experiments on free convective heat transfer from side walls of a vertical square cylinder in air," *Experimental Thermal and Fluid Science* 29, 1-8, 2004.

- [27] Li, P., Xu, b., Han, J., and Yang, Y., “Verification of a model for thermal storage incorporated with an extended lumped capacitance method for various solid-fluid structural combinations,” *Solar Energy* 105, 71-81, 2014.
- [28] Jambunathan, K., Lai, E., Moss, A., and Button, B.L., “A review of heat transfer data for single circular jet impingement,” *International Journal of Heat and Fluid Flow* 13, 106-115, 1992.
- [29] Dupin, J.J and Joshua, S., ‘Analogies and “Modeling Analogies” in Teaching: Some Examples in Basic Electricity,’ *Science Education* 73, 207-224, 1989.
- [30] Robertson, A.F. and Gross, D., “An Electrical-Analog Method for Transient Heat-Flow Analysis,” *Journal of Research and National Bureau of Standards* 61, 105-115, 1958.
- [31] Infineon Technologies, *Thermal Resistance Theory and Practice*. Infineon Technologies AG, Munich, Germany 2000.
- [32] Doebelin, E.O. *Measurement Systems: Application and Design 3rd Ed*. McGraw-Hill, New York, NY 1983.
- [33] Gu, S., Lu, T.J., and Evans, A.G., “On the design of two-dimensional cellular metals for combined heat dissipation and structural load capacity,” *International Journal of Heat and Mass Transfer* 44, 2163-2175, 2001.
- [34] Zhang, L. and Chen, Z., “Convective heat transfer in cross-corrugated triangular ducts under uniform heat flux boundary conditions,” *International Journal of Heat and Mass Transfer* 54, 597-605, 2011.
- [35] Schneider, G.E., and LeDain, B.L., “Fully Developed Laminar Heat Transfer in Triangular Passages,” *Journal of Energy* 5, 15-21, 1981

Appendix A: Digital Image Correlation

A.1 Digital Image Correlation Fundamentals

Digital Image Correlation (DIC) is an imaging technique which offers an alternative method of measuring deformation and strain of test specimen without applying physical sensors, such as strain gages or extensometers, to the specimen itself. Additionally, this technique yields a full field of measurements over the region which the images capture. In contrast, strain gages and extensometers only allow measurements to be taken at selected locations. Therefore, DIC yields more complete results, and allows tests to be conducted without any interference that may be caused by the application of physical sensors to a test specimen.

The concept of DIC is rooted in making digital comparisons of images taken in succession during a period of time over which a test specimen is loaded. The specimen must be painted with a variable speckle pattern such that its surface has a may be divided into small subsets each with a unique grayscale intensity value. This intensity serves essentially serves as a fingerprint, uniquely identifying each subset [A1]. The geometric arrangement of these subsets may then be compared from one image to the following image in succession to determine how the subsets may have shifted. The matching of subsets from one image to the next is performed via a correlation algorithm [A2].

A.1.1 Stereoscopic Imaging

Although DIC analysis may be performed based on images taken with a single camera, collection a full three-dimensional deformation and strain field of a specimen under loading requires, at minimum, a dual-camera system [A3]. In this case, the images taken from each camera must overlap each other. DIC analysis can only be performed within that overlap region. Much like with two-dimensional DIC, each image from each camera must be compared to the previous, or reference, image by correlating grayscale intensities from the subsets of the images [A4].

A.1.2 DIC Testing Methods

A speckle pattern was painted onto the upper surface of each specimen for the purpose of taking DIC measurements of deformation and strain. Each specimen was spray painted with a white base paint, capable of sustaining temperatures up to 1200°F. Black speckles were then added onto this white base using the same variety of paint. Past studies of DIC analysis have shown that best results are yielded when the size of each speckle (on average) is approximately $1/3 - 1/5$ the scale of the smallest anticipated deformation. Although, it is also crucial that the speckles not be uniform or show any discernible patter of application [A3]. Therefore, the sizes of the individual speckles may range a slightly larger expanse than $1/3 - 1/5$ the scale of the deformation. Estimations of deformation for the purposes of this work were made based on simple thermal expansion and idealization of jet pressure each

specimen, as a point on a simply supported beam. The smallest expected scale of deformation was on the order of $1/1000^{\text{th}}$ of an inch.

Although it was the intention of the study to paint speckles small enough to fit 3 to 5 speckles within a $1/100^{\text{th}}$ inch diameter, it was found during set up that this was not possible with the painting method used. When spray painting, the largest drops of paint, which will become the largest speckles when they fall on the painting surface, fall closest to the spray nozzle. Meanwhile the smallest drops of paint remain airborne longer, and thus land further from the spray nozzle. The painter must determine what distance from the spray can nozzle yields speckles of the desired size. In this study, unfortunately, it was found that droplets small enough to produce appropriately speckles were airborne long enough to almost fully dry before landing on the painting surface. As a result, using this method, it was not possible to paint speckles of the desired size onto the specimen which would not simply land as dust and blow away or smudge with touch. In this study, the smallest possible speckles were painted onto the specimen without exceeding the limit at which the paint would dry midair. As a result, it is the speckles were much larger than the desired $1/3000^{\text{th}}$ - $1/5000^{\text{th}}$ inch in size. The consequence of this is that resolution is lost, and deformations on the order of $1/1000^{\text{th}}$ inch could not be perceived by the system. An alternative solution to this resolution issue is to decrease the field of view of the cameras. However, decreasing the field of view any further would reduce it to a size which did not capture key locations of interest, specifically weld lines. A zoomed clip of the speckle pattern on Test Specimen 2 is shown in Figure A.1.

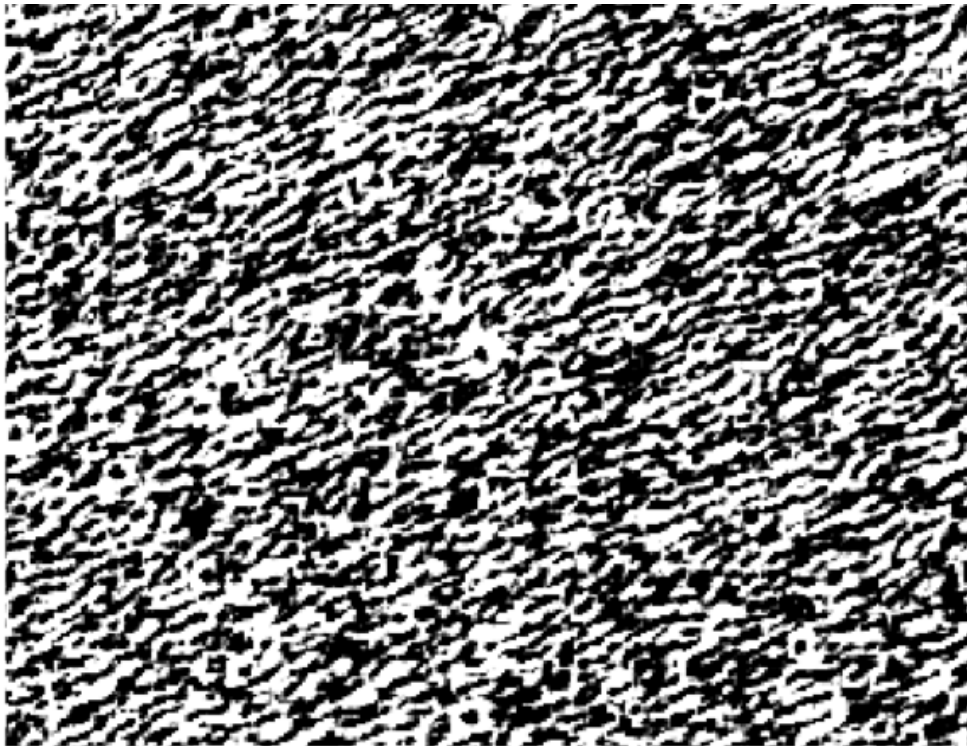


Figure A.1: Speckle Pattern on Test Specimen 2

A.1.3 Imaging Equipment & Configuration

Two high speed pco.edge scientific CMOS (complementary metal-oxide semiconductor) cameras were used to collect images of each test specimen during testing to use in DIC analysis of the specimen behavior. The main features and specifications of these cameras as outlined in their user manual may be seen in Table A1 below [A5].

Table A1: pco.edge sCMOS Camera Specifications

| Noise | Resolution | Dynamic Range | Shutter Speed |
|---------------|----------------|---------------|---------------|
| 1.4 electrons | 5.5 megapixels | 22000:1 | 100 fps |

Nikon zoom lenses were attached to these cameras and set for a focal length of 210 mm. Aperture was set to an F-stop setting of 8. Furthermore, since the cameras had to be set at a relatively large angle with respect to their subject, scheimpflugs were installed between the camera and the lenses to improve depth of field. Finally, the field of view of these cameras was adjusted such that, on average, approximately 3 pixels spanned a single speckle on each test specimen. Based on the resolution of the camera, this results in a field of view of approximately 5.75” x 4.00”. Each camera was set to this specification. Positioning of these cameras with respect to the test specimen and VT Hot Jet are depicted in Figure 11.

3.7.3 Processing and Results of DIC Images

Images were taken by each sCMOS camera directly before the application of the thermal load and at the instant when the thermal load was removed. A Matlab code was developed to assess the correlation between a two images in sequence. Using this code it was determined that the set of chronological DIC images discussed above exhibited excellent correlation. Therefore, the software was able to identify the same structures, or speckles in this case, from one image to the next. The calibration images taken prior to each test were then imported into in DaVis 8.2.3 StrainMaster and calibrated based on a 3rd-order polynomial model [A6]. The test images were then imported into the StrainMaster software for processing. Subsets were 64 x 64 pixels in size, with an overlap of 75%. Images were processed such that the images taken directly after the hour of thermal loading were referenced against the pre-loading. This gives strain map results after the loading cycle. The ϵ_{xx} and ϵ_{yy} strain maps from each set for each specimen were then examined qualitatively for clear strain patterns. In Figures A.1 and A.2, it is clear that there is very low strain percentage in either the ϵ_{xx} and ϵ_{yy} . However, more importantly, there are no clear patterns, indicative of physical deformation. It appears that each of this images presents nothing more than system noise. Due to the concerns for lack of resolution discussed above, it is believed at this point that no clear, significant strain patterns were detected during this testing. Very similar results are seen in Figures A.3 and A.4 for Test Specimen 2.

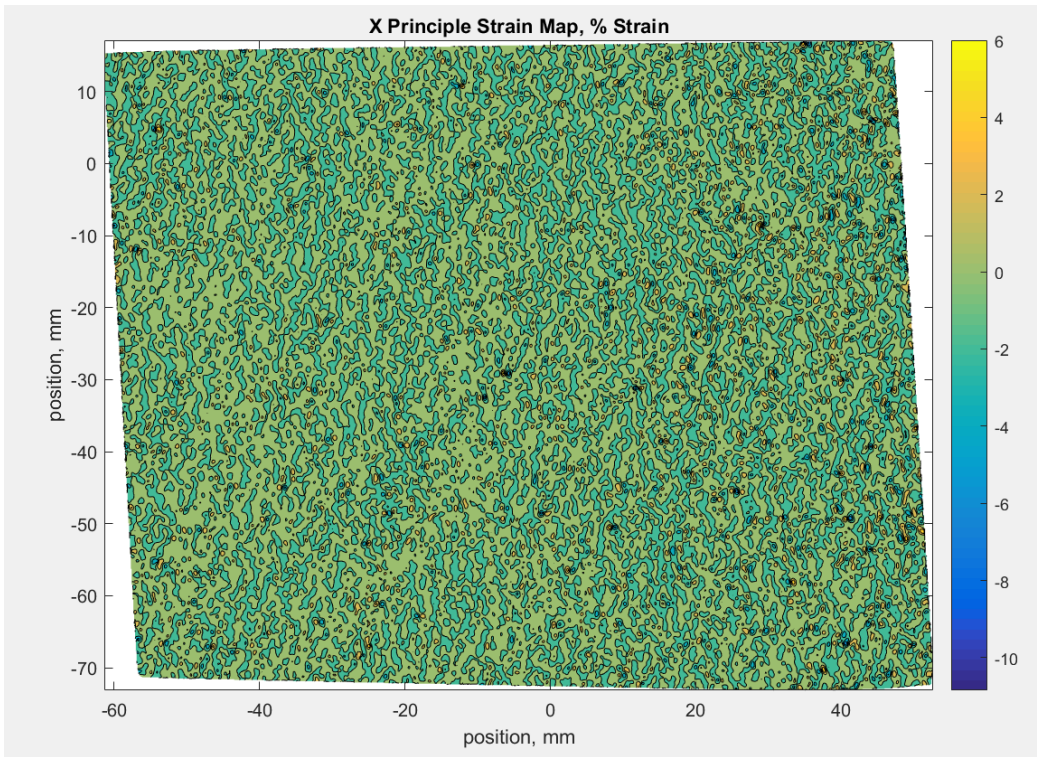


Figure A1: ϵ_{xx} Strain Map of Test Specimen 1 after Thermal Loading

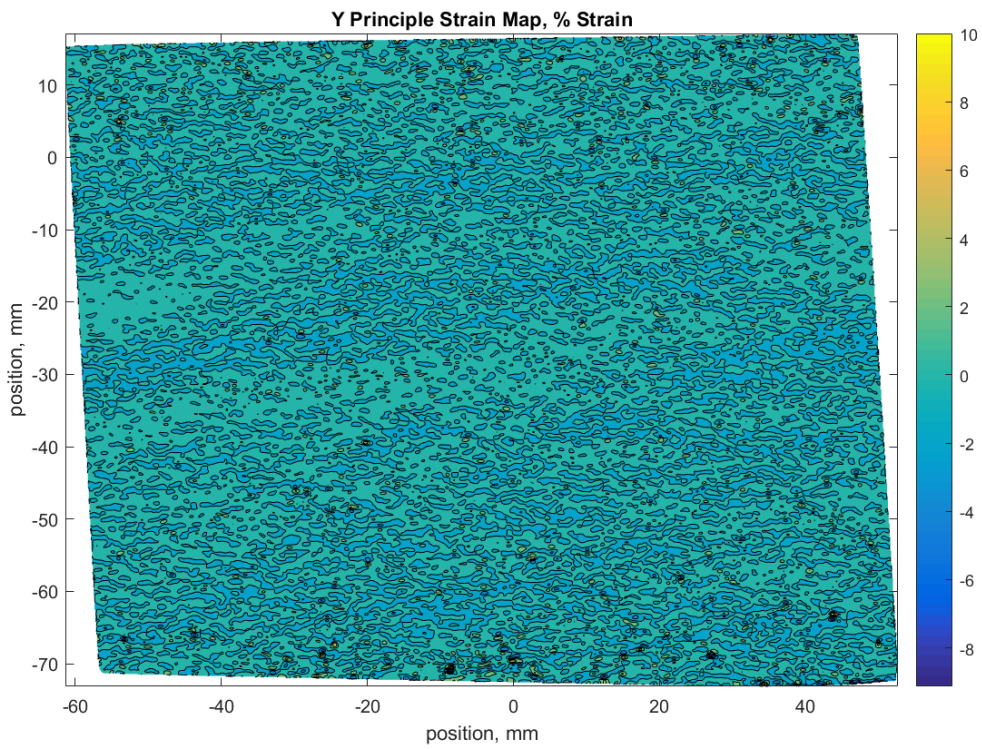


Figure A2: ϵ_{yy} Strain Map of Test Specimen 1 after Thermal Loading

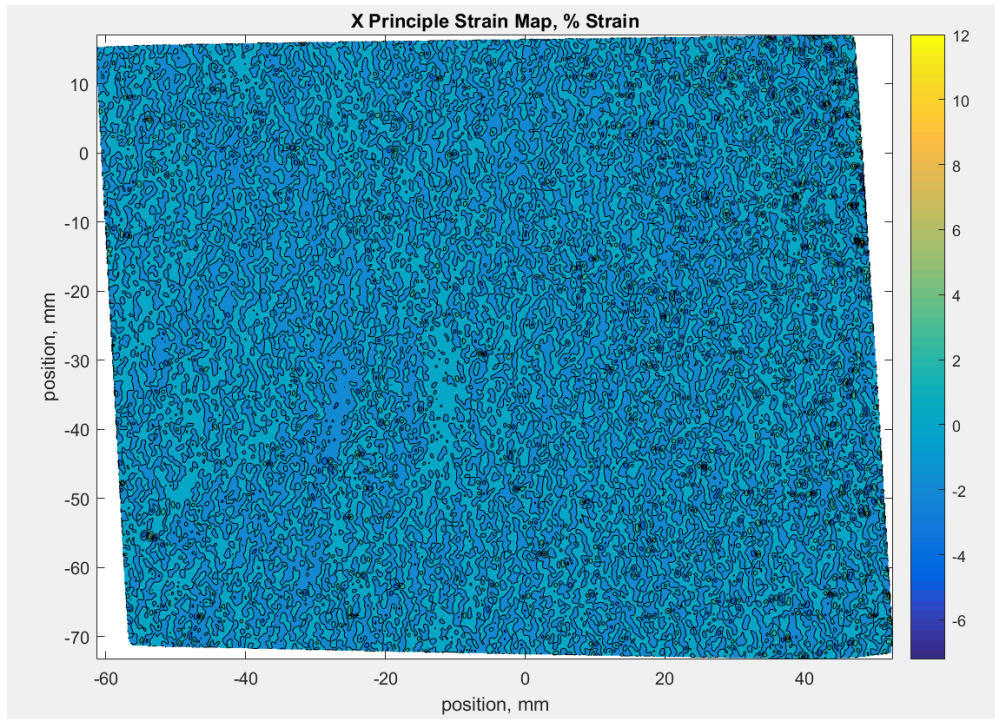


Figure A3: ϵ_{xx} Strain Map of Test Specimen 2 after Thermal Loading

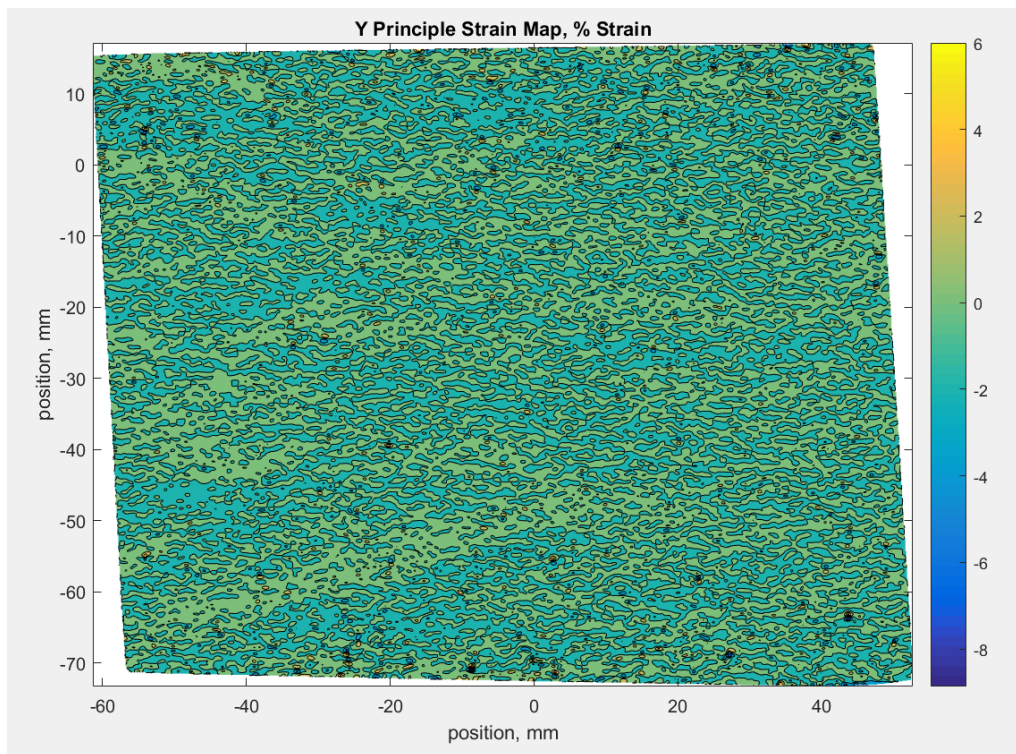


Figure A4: ϵ_{yy} Strain Map of Test Specimen 2 after Thermal Loading

Appendix A References

[A1] Helfrick, M., “An Investigation of 3D Digital Image Correlation for Structural Health Monitoring and Vibration Measurement”, MS Thesis, Department of Mechanical Engineering, University of Massachusetts Lowell, Lowell, MA, July. 2008.

[A2] Leung, C., “Examination of Braided Composite Geometric Factors Using Three Dimensional Digital Image Correlation Measurement Techniques”, MS Thesis, Mechanical Engineering Department, University of Alberta, Edmonton, Alberta, CA, 2012.

[A3] Sutton, M.A., Orteu, and J. Schreier, H.W., *Image Correlation for Shape, Motion and Deformation Measurements*, Springer Science + Business Media, LLC, New York, NY 2009.

[A4] “StrainMaster Product Manual”, LaVision GmbH, Göttingen, Germany, Aug. 2011.

[A5] PCO AG, “pco.edge User Manual”, Kelheim, Germany, 2011.

[A6] LaVision GmbH. *DaVis StrainMaster, Release 8.2.3.*